Determining Optimum Imaging Parameters for SWIFT: Application to Superparamagnetic Iron Oxides and Magnetized Objects

A DISSERTATION
SUBMITTED TO THE FACULTY OF THE GRADUATE SCHOOL
OF THE UNIVERSITY OF MINNESOTA
BY

Robert Daniel O'Connell

IN PARTIAL FULFILLMENT OF THE REQUIREMENTS
FOR THE DEGREE OF
DOCTOR OF PHILOSOPHY

Michael Garwood, PhD., Adviser

June 2011

Acknowledgements

First I would like to thank my adviser Michael Garwood for his guidance and support. I am grateful for his tutelage and the effort he made to join the physics department so that I could work under him at the Center for Magnetic Resonance Research at the University of Minnesota. His enthusiasm and unique insight into MRI made my doctoral experience both educational and enjoyable.

I would also like to thank my committee members E. Dan Dahlberg, Alex Kamenev, E. Russell Ritenour, and Gregory Metzger. Their advice and support were very helpful.

This work would not have been possible without the assistance of the Garwood group. I give special thanks to Curt Corum, Steen Moeller, Djaudat Idiyatullin, Angela Snyder, Ryan Chamberlain, Malgorzata Marjanska, Shalom Michaeli, and Jang-Yeon Park. I would not have been able to complete this work without their help and support.

On a personal note, I want to thank my wife, Maria, for her patience, support, and understanding throughout the PhD process. I want to thank my parents, Mark and Donna, for their encouragement through all of my years of education. I also want to thank my children, Alec and Kellen, for helping me to get through the tough times.

For my wife, Maria
and sons, Alec and Kellen

Table of Contents

Table of Tables

Table of Figures

1. Introduction

Magnetic resonance imaging (MRI) is a powerful tool that is used to non-invasively visualize internal structures. MRI uses a strong magnetic field to excite water molecules and then uses sensitive coils to measure how the molecules behave after excitation. The water molecules behave differently depending on what type of structure they are in, e.g. fat, bone, and muscle. There are many structures, such as muscle and fat, that image very well with conventional MRI techniques, such as the spin-echo and gradient echo. However, there are some structures, such as bone and plastics, which are not imaged well with conventional techniques because the signal decays before it can be measured. There are two important time constants that affect the amount of signal that a structure has: the longitudinal (T_1) and transverse (T_2) relaxation times. A short T_1 yields a large signal, whereas a short T_2 yields a small signal. There are many new techniques that are being used to image objects with short T_2, including BLAST [1], RUFIS [2], UTE [3-5], SPRITE [6-8], and the relatively new sequence known as SWIFT, SWeep Imaging with Fourier Transformation [9, 10]. All of these sequences have some modicum of success, but this work is only considering the imaging properties of SWIFT.

The ideal sequence for measuring ultra-short T_2 spins comprises a series of infinitely short excitation pulses (δ-pulses) followed immediately by acquisition, with no delay in between. However, this sequence cannot be practically realized since excitation pulses have finite duration (T_p) and time is required for scanner electronics to switch between transmit and receive modes. Furthermore, there is signal loss due to T_2 effects [11] and an effective flip angle reduction due to off-resonance effects during a pulse of

finite duration [12]. SWIFT comes close to offering many of the desirable features of this theoretical δ-pulse sequence.

SWIFT utilizes a swept radiofrequency excitation of the nuclear spins coupled with time-shared signal acquisition to image objects. The negligible time between excitation and signal acquisition affords the opportunity to image objects with extremely fast transverse relaxations.

There are various ways that the T_1 and T_2 of a structure can be manipulated to create desired effects. Contrast agents are often used to identify areas of interest by altering the T_1 and T_2 of the targeted area. Superparamagnetic iron oxides (SPIOs) are magnetic nanoparticles that are used as contrast agents in MRI for cancer detection and cellular and molecular imaging. The external magnetic field induces a magnetic field from the SPIO which causes a field inhomogeneity in the surrounding area. The water particles in this area experience a T_1 and T_2 shortening. These effects are well predicted in outer-sphere theory as introduced by Gueron [13] in 1975 and refined by Gillis et al. [14, 15] in several papers in the late 1990's. This relaxation is referred to as Curie relaxation in reference to the Curie-Brillouin law of paramagnetic materials. The inhomogeneous field leads to alterations of the water molecules' Larmor frequencies which causes dephasing in the transverse plane, reducing the net signal when evaluated using traditional MRI techniques. The inhomogeneous fields also cause frequency shifting of signals in MRI images, leading to pileup artifacts and signal voids [16, 17]. SWIFT is ideal for imaging SPIO's. In SWIFT, the signal is T_1 sensitive and T_2 insensitive, causing signal amplification instead of a reduction as in other techniques. Simply, instead of dark spots the SPIO causes the voxels to become bright spots. Positive contrast allows for

more accurate identification of the targeted areas as well as retaining the anatomical information.

The purpose of this work is to determine the optimum parameters for imaging with SWIFT. The complexity of the SWIFT sequence makes it very difficult to solve analytically for all relaxation times and excitations. This work will present a means of approximating the signal energy from the SWIFT sequence without solving for it directly by comparing SWIFT to the δ-pulse sequence. Equations for maximum energy and contrast will be determined.

The predictive equations for SWIFT will then be extended to optimize the imaging of SPIOs. The effects of particle size, concentration, and magnetization on signal magnitude will be discussed. Pulse sequence parameters will be determined to optimize signal amplitude and contrast for the system.

Imaging with SWIFT around magnetized objects, such as medical implants, leads to pileup artifacts surrounding signal voids, susceptibility artifacts. These susceptibility artifacts distort the image, leading to improper representation of the surrounding area. In the case of medical implants, the information about the surrounding anatomy is lost. Pileup artifacts will also be investigated to determine the parameters that control their size and shape as well as a method to correct these artifacts.

These goals will be accomplished primarily through the use of a home made Bloch simulator to numerically model the system. Analytical solutions will be derived from first principals and compared to the numerically modeled solutions. The determined equations will then be verified through experiment.

2. Fundamentals of MRI and SWIFT

2.1 The Larmor Frequency and Equilibrium Magnetization

This is a brief overview of nuclear magnetic resonance. For a more comprehensive explanation please refer to a text such as *Spin Dynamics* by Malcolm Levitt [18].

Certain atoms (e.g. Hydrogen) have two features that make NMR possible: spin and magnetic moment. In the presence of an external magnetic field (B_0), conventionally in the *z*-direction, Zeeman splitting will occur, and a given nucleus will have either a spin-up or spin-down magnetic moment. For the case of spin ½ particles there will be two energy levels separated by equation 2.1, where ω_0 is defined as the Larmor frequency, γ is the magnetogyric ratio, and μ is the magnetic moment.

$$\hbar\omega_0 = 2\mu B_0 = \gamma\hbar B_0 \qquad (2.1)$$

The nuclear magnetic moment will precess around the direction of the external field at a rate equal to the Larmor frequency. Figure 2.1 illustrates a) Zeeman splitting and b) a spin-up and spin-down magnetic moment precessing around an external magnetic field.

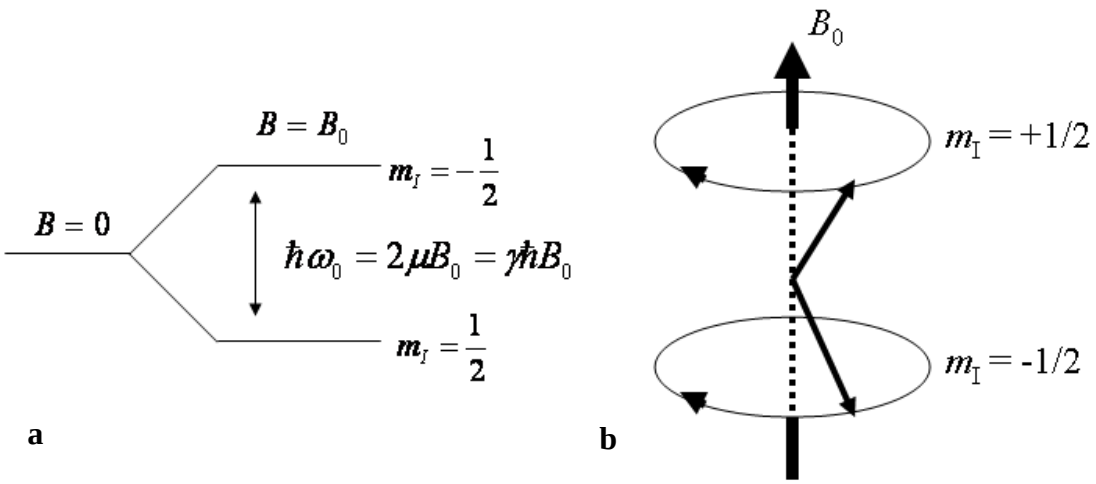

Figure 2.1: A spin placed in an external magnetic field (B_0) will experience Zeeman splitting where it can have two possible energy levels separated by an energy that is proportional to the Larmor frequency ω_0, either spin-up or spin-down. b) The magnetic moment will then precess around B_0 at a frequency of ω_0.

An ensemble of nuclei will have both spin-up and spin-down nuclei, but the net magnetic moment of the system will form along the direction of the external field and can be described by equation 2.2, where M_0 is the magnetization in thermal equilibrium, μ is the magnetic moment, N is the total number of spins, B is the external magnetic field, k_B is Boltzmans's constant, and T is the temperature.

$$M_0 = \left(N_\uparrow - N_\downarrow\right)\mu = N\mu \tanh\left(\mu B \big/ k_B T\right) \tag{2.2}$$

2.2 Excitation, Relaxation and the Bloch Equations

The magnetization is said to be excited when it is rotated out of thermal equilibrium. Excitation occurs when an additional magnetic field is applied that is oscillating at the Larmor frequency of the nuclei. This field is called the RF field. When the RF field is turned on the net magnetic moment will precess around it. It is convenient to work in a reference frame that is rotating around the *z*-axis at the Larmor frequency. In

the rotating frame the RF field that is oscillating at the Larmor frequency will appear to be a constant field. The rest of this work will be done in this first rotating frame unless otherwise stated.

The most basic RF pulse is a pulse with constant amplitude (B_1) and duration (T_p). The magnetization will rotate around the RF field through an angle θ as defined by equation 2.3.

$$\theta = \gamma B_1 T_p \tag{2.3}$$

A pulse with large B_1 and short T_p is called a hard pulse. A pulse with small B_1 and long T_p is called a soft pulse.

Adiabatic pulses, such as the hyperbolic secant pulse (HSn), have the desirable feature that all spins with frequencies within the excitation bandwidth (*bw*) are excited with the same flip angle [19]. The HSn pulse is described in amplitude and frequency modulation by equations 2.4 and 2.5, ω_1 is the amplitude, t is time, β is a scaling factor, and ω_{RF}-ω_c is the frequency modulation. Hard pulses have off-resonance effects that lead to reduced flip angles. Figure 2.2 is a plot comparing excitation profiles of hard pulses and HSn pulses.

$$\omega_1(t) = \omega_1^{\max} \operatorname{sec} h\left(\beta\left(2t/T_p - 1\right)\right) \tag{2.4}$$

$$\omega_{RF}(t) - \omega_c = A \tanh\left(\beta\left(2t/T_p - 1\right)\right) \tag{2.5}$$

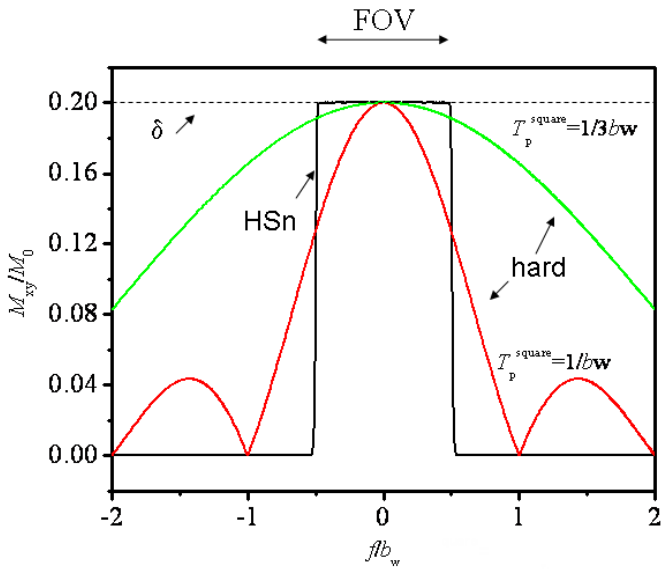

Figure 2.2: Excitation profiles of hyperbolic secant (HSn) and hard pulses (at pulses times of 1/*bw*, 1/3*bw*, and 0 (δ-pulse)) as a function of frequency [10]

The HSn pulse has uniform excitation over the bandwidth. The hard pulses do not have uniform excitation over the same bandwidth. In order for the hard pulse to have a uniform excitation over the bandwidth it must have a pulse time that is significantly shorter than 1/*bw*, with the perfect scenario being an infinitely short pulse.

When the RF field is turned off the magnetization will return to thermal equilibrium. The magnetization along the *z*-axis will return to thermal equilibrium at a rate proportional to T_1, the longitudinal relaxation rate. The magnetization in the transverse (*xy*) plane will exponentially decay to zero at a rate proportional to T_2, the transverse relaxation rate. Values of T_2 are always less than or equal to T_1. Figure 2.3 illustrates the a) T_1 and b) T_2 time constants after some excitation.

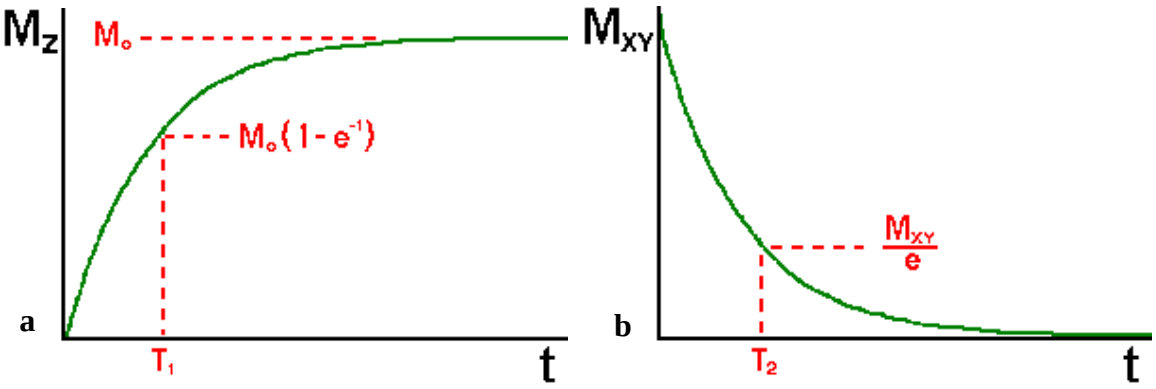

Figure 2.3: After excitation, a) magnetization along the *z*-axis will return to thermal equilibrium at a rate proportional to T_1. b) Magnetization in the *xy*-plane will decay to zero at a rate proportional to T_2.

Longitudinal (T_1) relaxation occurs due to small localized magnetic fields. A single spin in a large external magnetic field would precess around the field indefinitely. The thermal equilibrium magnetization will occur because each spin experiences a slightly different external magnetic field than its neighbors due to additional fields caused by the movement of electrons and protons. This field changes over time and leads to the breakdown of the precessional rotation cone. Each spin will sample all of the different orientations but not isotropically. It is more likely that the spins will be driven toward the direction of lowest energy, parallel to the large external field. When the moments from all spins in the system are summed, a net moment along the *z*-axis is formed and will maximize at the thermal equilibrium value, even though the magnetization from each individual spin is fluctuating.

Transverse (T_2) relaxation occurs due to the dephasing of spins in the *xy*-plane. It is impossible for the spins to remain perfectly synchronous while rotating. As the spins become more and more out of phase, the net magnetic moment in the *xy*-plane will decay

because the individual magnetic moments will cancel each other. Eventually the spins completely dephase and the transverse magnetic moment decays to zero.

T_2 is the natural inherent relaxation time constant of a structure. There are other factors that can cause decay in the transverse magnetization. T_2' is used when the effect of dephasing is due to external field inhomogeneities. The different transverse relaxation rates are combined to form T_2*, which is expressed in equation 2.6

$$\frac{1}{T_2^*} = \frac{1}{T_2} + \frac{1}{T_2'} \tag{2.6}$$

The equations of motion for the system are described by the Bloch equations. Conveniently, the net magnetic moment can be treated classically, rather than quantum mechanically. In the presence of a magnetic field a magnetic moment will experience a torque which causes a change in the angular momentum, as described by equation 2.7. The Bloch equations are derived when the conditions for thermal equilibrium are imposed on equation 2.7. The Bloch equations are given in equations 2.8-2.10.

$$\hbar(d\mathbf{I}/dt) = \boldsymbol{\mu} \times \mathbf{B_1} \rightarrow d\mathbf{M}/dt = \gamma \mathbf{M} \times \mathbf{B_1} \tag{2.7}$$

$$\frac{dM_z}{dt} = \gamma(M_x B_y - M_y B_x) - \frac{(M_z - M_0)}{T_1} \tag{2.8}$$

$$\frac{dM_x}{dt} = \gamma(M_y B_z - M_z B_y) - \frac{M_x}{T_2} \tag{2.9}$$

$$\frac{dM_y}{dt} = \gamma(M_z B_x - M_x B_z) - \frac{M_y}{T_2} \tag{2.10}$$

2.3 Signal

The NMR signal (S) is derived by temporally acquiring the transverse magnetization after excitation. Typically, the magnetization is excited with a series of pulses where each pulse is repeated after some time T_R. The magnetization behavior will eventually repeat after each excitation, reaching a steady state. The steady state S will then be acquired in the time between one excitation and the next. The two most common signal acquisitions are the free induction decay (FID) and the echo, shown in figure 2.4.

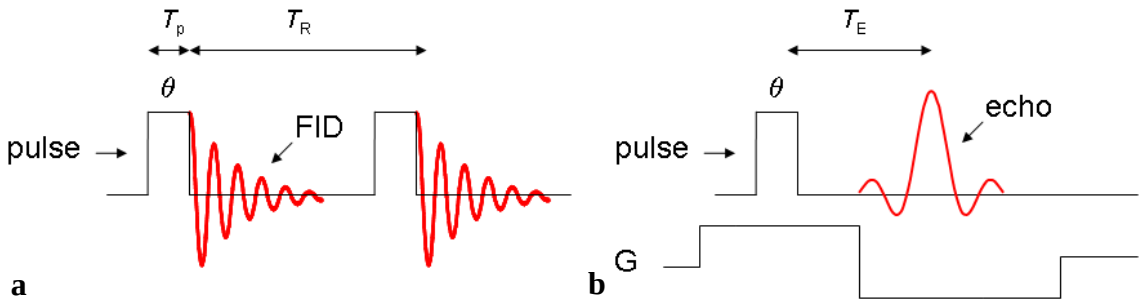

Figure 2.4: A pulse diagram of a hard pulse followed by a) a free induction decay and b) and echo.

The FID is a measurement of S immediately after excitation. An echo is a refocusing of S some time after excitation. The echo shown in figure 2.4b is a gradient echo which uses an additional linear external magnetic field to change the Larmor frequency of each nucleus in space. The spins will dephase in the xy-plane because they are rotating at different frequencies. The gradient magnitude is then flipped, causing the spins to refocus at some later time T_E. A pulse sequence is said to be spoiled when the transverse magnetization is zero before each pulse.

2.4 Imaging

A one-dimensional (1D) object can be defined as a series of magnetizations along the x-axis, with spin density $\rho(x)$. A field gradient ($G(x)$) is applied to the system in order to spatially encode the magnetizations with a distinct resonance frequency. The Larmor frequency at each point is defined by equation 2.11.

$$\omega_0(x) = \gamma(Gx + B_0) \tag{2.11}$$

After excitation the acquired data is placed in a Fourier plane, known as k-space. The number of data points in k-space is the same as the number of points acquired. The spacing between each k-space point (Δk) is defined by equation 2.12 where L is the length of the object.

$$\Delta k = \frac{1}{L} \tag{2.12}$$

The resolution (Δx) of the object is defined by equation 2.13, where k_{max} is the dimension of k-space.

$$\Delta x = \frac{1}{k_{max}} \tag{2.13}$$

The k-space data is then Fourier transformed to recover $\rho(x)$.

An FID will fill k-space starting at k=0 and ending at k=k_{max}. An echo sequence will acquire both positive and negative frequencies, so k-space will be filled from negative to positive. The data on the left side of the lobe will fill the negative k-space, the center of the lobe will fill the center (k=0) and the right side will fill positive k-space. The additional frequency information obtained in the echo sequence creates a more accurate representation of the object upon FT.

Imaging 3D objects is a simple extension of the 1D method with the inclusion of phase encoding gradients in the *y* and *z* directions. The phase encoding gradients move the acquisition to a specific line in *k*-space and the line is then filled in the frequency encoded direction. The phase encoding gradients are then changed for the next acquisition and another line of *k*-space is filled. A 3D Fourier transform is performed on the data after *k*-space has been completely filled, creating an image of the object..

2.5 SWIFT

The Garwood group has developed a new method that is known as SWIFT, sweep imaging with Fourier transformation [9, 10]. The ideal SWIFT sequence is continuous with time-shared excitation and acquisition. SWIFT is a spoiled pulse sequence. Due to hardware limitations it is not currently possible to both excite and acquire at the same time, though advances are being made to make a continuous SWIFT sequence a reality. Gaps are inserted into the pulse so that the signal can be acquired in-between excitations. The signal is a pseudo-FID, not a true FID, due to the concurrent excitation imposing an additional phase upon the signal. Figure 2.5 is a diagram of the SWIFT pulse sequence.

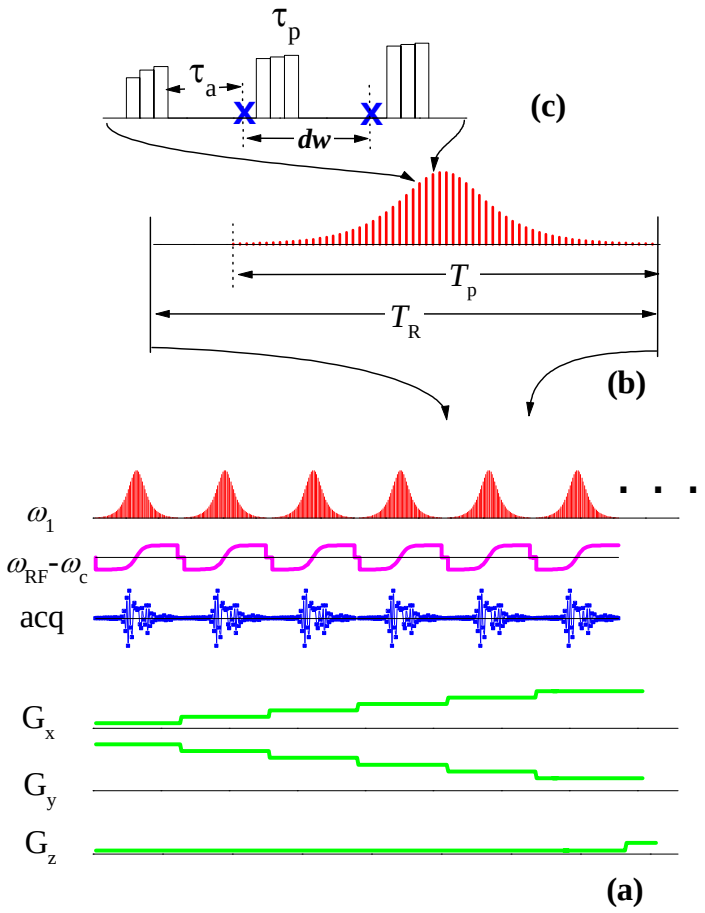

Figure 2.5: The SWIFT pulse sequence (a) detailed presentation of the repeated part of the sequence (b) magnified presentation of pulse segments (c) magnified pulse steps. The data is acquired at the points marked with a blue *x*. [8]

SWIFT is composed of a series of adiabatic hyperbolic secant (HSn) RF pulses. The HSn pulse utilizes both amplitude and frequency modulation. The amplitude of the pulse is denoted by the variable $\omega_1=\gamma B_1$ where γ is the gyromagnetic ratio. The instantaneous frequency of the pulse is denoted by ω_{RF}-ω_c and manifests as a phase shift in the rotating reference frame. The pulse is divided into *N* segments which are stepped in amplitude in order to preserve adiabaticity over the segment time τ_p. The pulse is

executed in the presence of a magnetic field gradient $\boldsymbol{G}=(G_x\mathbf{i}+G_y\mathbf{j}+G_z\mathbf{k})$, imparting a spatially dependent Larmor frequency where equation 2.1 now becomes

$$\omega_0(r)=\gamma(\boldsymbol{G}\cdot\boldsymbol{r}+B_0) \tag{2.14}$$

The signal is acquired at the times designated by an 'x' in Figure 2.5c at time τ_a after each pulse segment and separated by a dwell time given by $dw=\frac{T_p}{N}$ where T_p is the total pulse time, typically in the millisecond range. This method is extremely sensitive to materials with short T_2 times because the signal acquisition is interwoven with the excitation pulse.

The signal from a SWIFT sequence is contaminated with the phase of the RF pulse. The phase can be removed by the convolution process given by

$$r(t)=h(t)\otimes x(t) \tag{2.15}$$

where $r(t)$ is the measured response, $x(t)$ is the pulse, and $h(t)$ is the desired FID. A convolution in the time domain is a complex multiplication in the frequency domain. $h(t)$ may be recovered by

$$h(t)=FT\left(H(\omega)\right)=FT\left(\frac{R(\omega)X^*(\omega)}{\left|X(\omega)\right|^2}\right) \tag{2.16}$$

To create an image, SWIFT fills *k*-space radially with the corrected FID. Each radial spoke is defined by the direction of the field gradient and fills starting at k=0 and moving radially outward. The data is then gridded [20] and 3D Fourier transformed to obtain a 3D image.

3. Optimization of SWIFT

3.1 Introduction

The goal in MRI is to acquire as much information as possible from the measured objects. It is therefore important to be able to determine optimum parameters before scanning so that the images will have the maximum signal for targeted spins or maximum contrast between two spins that need to be compared. Determining optimum parameters for imaging an object requires knowing how a spin will behave during and after RF excitation. However, the Bloch equations are non-linear differential equations and are not directly solvable. The Bloch equations need to be simplified by making significant approximations to eliminate terms and by using the steady state condition in equation 3.1.

$$\boldsymbol{M}(t) - \boldsymbol{M}(t + T_R) = 0 \tag{3.1}$$

The simplest scenario is that of a constant RF pulse in the first rotating frame. Using the condition that $d\boldsymbol{M}/dt = 0$, the Bloch equations can be solved to find the steady-state magnetization vector, given by equations 3.2, for an RF field along the *x*-axis.

$$M_x = 0 \qquad M_y = \frac{\omega_1 T_2 M_0}{1 + T_1 T_2 \omega_1^2} \qquad M_z = \frac{M_0}{1 + T_1 T_2 \omega_1^2} \tag{3.2}$$

With these equations a spin's behavior can be predicted based on its relaxation constants and the RF pulse magnitude [21].

The steady state signal for the ideal spoiled δ-pulse sequence is predicted by the Ernst equation [22], given by equation 3.3. The Ernst equation is derived by assuming that there is no relaxation during the infinitely short pulse and that there is no magnetic field when the spin is relaxing. The condition is then imposed that the *z*-magnetization

before the pulse and the *z*-magnetization after the pulse and acquisition time need to be equal. The signal is then calculated as being the component of the *z*-magnetization before the pulse that is rotated into the *xy*-plane by the pulse. By integrating equation 3.3 over the entire acquisition time we arrive at equation 3.4, the signal energy equation.

$$S = dc\frac{M_0 \sin(\theta)\left(1-E_1\right)}{(1-\cos(\theta)E_1)}e^{-t/T_2} \tag{3.3}$$

$$S^2\left(\theta\right) = dc\frac{M_0^2 T_2 \sin^2(\theta)(1-E_1)^2}{2T_A(1-\cos(\theta)E_1)^2}(1-E_2^2) \tag{3.4}$$

where θ is the flip angle, *dc* is the acquisition duty cycle, $E_1 = \exp(-T_R/T_1)$, $E_2 = \exp(-T_A/T_2)$, T_R is the repetition time, and T_A is the acquisition time. The signal can be maximized for any given T_1 by exciting at a flip angle, the Ernst angle, as defined by equation 3.5.

$$\cos(\theta_{\max}) = E_1 \tag{3.5}$$

SWIFT is a very complicated pulse sequence for which there are not any approximations that can be made to make the Bloch equations easily solvable for all θ, T_1, and T_2. There is however another pulse sequence that closely resembles SWIFT that is known as RAFF (relaxation along a fictitious field) [23]. RAFF utilizes oscillating frequency and magnitude RF pulses with time-shared excitation and acquisition, equations 3.6 and 3.7. The magnitude and frequency components of SWIFT are similar to a sine and cosine curve from 0 to π respectively. By analyzing RAFF, which has a similar pulse sequence to SWIFT and concurrent excitation and acquisition, conclusions about SWIFT may be made.

$$\omega_1(t) = \omega_1^{\max} \left|\sin(\omega_1^{\max} t)\right| \tag{3.6}$$

$$\omega_{rf}(t) - \omega_0 = \Delta\omega = \omega_1^{\max} \cos(\omega_1^{\max} t) \tag{3.7}$$

Figure 3.1 illustrates the behavior of the effective RF field of RAFF as a function of time. The effective RF field starts along the *z*-axis and then rotates around the *y*-axis.

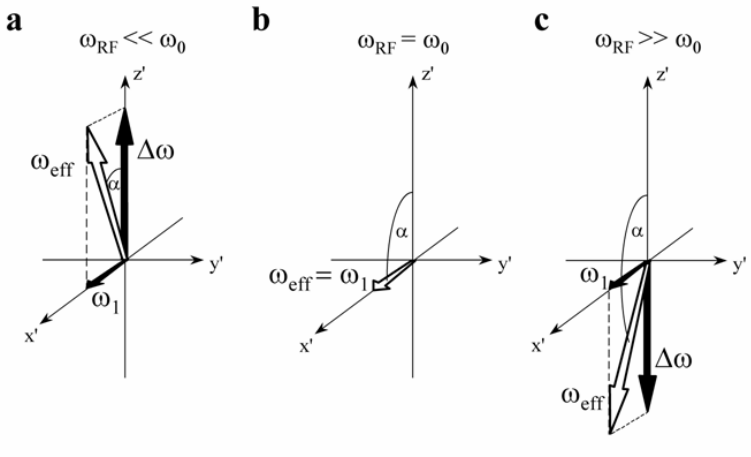

Figure 3.1: The RAFF effective RF field as it changes in time.

It is beneficial to think about this system in a reference frame that is rotating around the *y*-axis at the same rate as the RF field. Figure 3.2 illustrates this second rotating reference frame. In the second rotating frame the effective RF field is along the *z*′-axis and an additional fictitious field arises from the time derivative of the rotation.

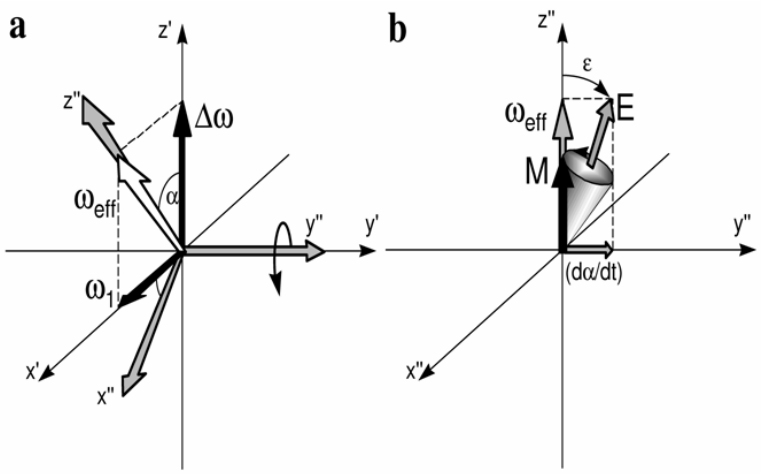

Figure 3.2: The RAFF RF field in the second rotating frame.

Equations 3.8-3.11 define the parameters shown in Figure 3.2. The resulting field in the second rotating frame is at a 45° angle from the z'-axis and is constant in magnitude.

$$\alpha(t) = \tan^{-1}\left(\frac{\omega_1(t)}{\Delta\omega_1(t)}\right) = \omega_1^{\max} t \tag{3.8}$$

$$\omega_{eff}(t) = \sqrt{\omega_1^2(t) + (\Delta\omega(t))^2} = \omega_1^{\max} \tag{3.9}$$

$$\varepsilon(t) = \tan^{-1}\left(\frac{\omega_{eff}}{d\alpha/dt}\right) = \frac{\pi}{4} \tag{3.10}$$

$$E_y = E_z = |E|\left(\frac{\sqrt{2}}{2}\right) = \frac{\omega_1^{\max}}{\gamma} \tag{3.11}$$

To solve for the steady state in the second rotating frame the Bloch equations need to be adapted to this frame, as defined in equations 3.12-3.14. For convenience the substitutions of $R_1=1/T_1$ and $R_2=1/T_2$ are used.

$$\frac{dM_x'}{dt} = M_y'\omega_z' - M_z'\omega_y' - R_2\cos\alpha\left[M_x'\cos\alpha + M_z'\sin\alpha\right] -$$

$$R_1\sin\alpha\left[M_0 + M_x'\sin\alpha - M_z'\cos\alpha\right] \tag{3.12}$$

$$\frac{dM_y^{'}}{dt} = M_z^{'}\omega_x^{'} - M_x^{'}\omega_z^{'} - R_2 M_y^{'} \tag{3.13}$$

$$\frac{dM_z^{'}}{dt} = M_x^{'}\omega_y^{'} - M_y^{'}\omega_x^{'} - R_2\cos\alpha\left[M_x^{'}\cos\alpha + M_z^{'}\sin\alpha\right] +$$

$$R_1\cos\alpha\left[M_0 + M_x^{'}\sin\alpha - M_z^{'}\cos\alpha\right] \tag{3.14}$$

Equations 3.12-3.14 can be simplified by applying equation 3.11 and by equating the relaxation constants to each other, R_1=R_2=R. Equations 3.12-3.14 then become equations 3.15-3.17.

$$\frac{dM_x^{'}}{dt} = \omega\left(M_y^{'} - M_z^{'}\right) - R\left(M_x^{'} + M_0\sin\alpha\right) \tag{3.15}$$

$$\frac{dM_y^{'}}{dt} = -M_x^{'}\omega^{'} - RM_y^{'} \tag{3.16}$$

$$\frac{dM_z^{'}}{dt} = M_x^{'}\omega^{'} - R\left(M_z^{'} - M_0\cos\alpha\right) \tag{3.17}$$

These equations can be solved by guessing that the solution will be sinusoidal. The magnetization components are defined in equations 3.18-3.21.

$$\rho = \frac{R}{\omega} \tag{3.18}$$

$$M_x^{'} = M_0\left[\frac{-5\rho^2 - 6\rho^4 - \rho^6}{1+7\rho^2+7\rho^4+\rho^6}\sin\alpha + \frac{-2\rho - 2\rho^3}{1+7\rho^2+7\rho^4+\rho^6}\cos\alpha\right] \tag{3.19}$$

$$M_y^{'} = M_0\left[\frac{2\rho+7\rho^3+6\rho^5+\rho^7}{1+8\rho^2+14\rho^4+8\rho^6+\rho^8}\sin\alpha + \frac{-3\rho^2-4\rho^4-\rho^6}{1+8\rho^2+14\rho^4+8\rho^6+\rho^8}\cos\alpha\right] \tag{3.20}$$

$$M_z^{'} = M_0\left[\frac{-\rho+\rho^5}{1+8\rho^2+14\rho^4+8\rho^6+\rho^8}\sin\alpha + \frac{4\rho^2+11\rho^4+8\rho^6+\rho^8}{1+8\rho^2+14\rho^4+8\rho^6+\rho^8}\cos\alpha\right] \tag{3.21}$$

This solution of RAFF shows that even an extremely simplified version of SWIFT results in a complex solution. The solution can not be used for SWIFT because it is not spoiled and the frequency sweep switches direction for each subsequent pulse. Moreover, the solution does not include relaxations where T_1 and T_2 are not equal.

3.2 Comparing SWIFT, the Ideal δ-pulse, and Hard Pulse Sequences

Without an analytical derivation that accurately describes the steady state SWIFT sequence we are forced to find an approximation equation. In SWIFT, a spin is excited when the frequency sweep reaches its Larmor frequency. It is excited very quickly and therefore closely resembles a δ-pulse. It has been proposed that SWIFT, like the δ-pulse sequence, can be described by the Ernst energy equation (3.4) [9]. In reality the δ-pulse can not be achieved as the pulse needs to have a finite duration, making it a hard pulse. In this section SWIFT, the δ-pulse, and hard pulse sequences will be compared using the Ernst energy equation (3.4) via a computer simulation program. Optimization equations for maximum energy and contrast will be determined from these comparisons. The equations will then be verified through experiment.

3.2.1 Methodology

The NMR system was modeled by using a Bloch simulator. The Bloch equations were numerically solved using the Runge-Kutta [23] method for three different types of sequences: 1) a δ-pulse, 2) a hard pulse, and 3) SWIFT for a single spin. The δ-pulse sequence used T_R = 4.045 ms and T_A = 4 ms with a 45 μs post-acquisition delay. The SWIFT sequence used T_p = 4 ms with 45 μs post-acquisition delay (giving T_R = 4.045 ms). For all simulations the acquisition bandwidth was 127 kHz. An ideal SWIFT sequence has simultaneous excitation and acquisition. However due to hardware

limitations, the signal must be acquired in gaps within the pulse sequence. Both gapped, with *dc* = 50%, and un-gapped simulations of SWIFT were done. T_p of the hard pulse was calibrated so that the pulse amplitude corresponded with the maximum pulse amplitude of the SWIFT pulse for a given θ, resulting in $T_p \leq 45$ μs. $T_A = 4$ ms was used. Simulations were completed for $T_2 \leq T_1$ for small T_1. The effect of having a resonance offset (ΔB_0) was also investigated. Additional simulations were completed with the δ-pulse and SWIFT to investigate the effects of changing T_R and T_A at constant flip-angle. Contrast evaluations were made for spins with similar T_1's. Figure 3.3 is an illustration of the simulated sequences

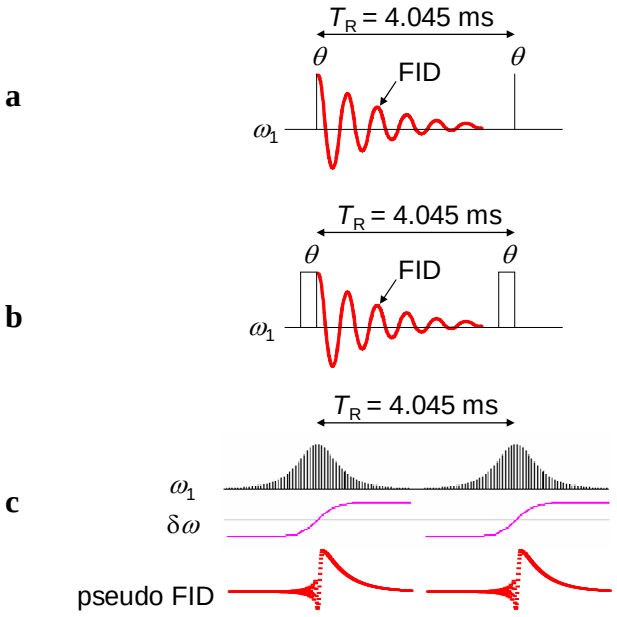

Figure 3.3: Illustration of simulated sequences. a) δ-pulse, b) hard pulse, c) SWIFT pulse

The gapping of the SWIFT pulse/acquisition leads to additional effects on the signal to noise ratio (SNR). SNR simulations were done for $T_2 < T_R/2$ for several scenarios: 1) δ-pulse with 512 points over the entire T_R; 2) δ-pulse with 256 acquired

points over the entire T_R; 3) δ-pulse with 256 acquired points over $T_R/2$; 4) 512-point SWIFT; and 5) gapped SWIFT (256 points, *dc* = 50%). An object with *bw* = 5 kHz was simulated at a 20^0 flip angle. Random noise was added to the time domain signal with $|\sigma| \leq 0.01$. The signal-to-noise ratio was evaluated in the frequency domain by taking the average of the object peak and dividing by the RMS of the off-peak signal.

Two experiments were done to test the validity of the simulations and the assertion that the SWIFT data can be described by the Ernst equations. The measurements were made on a 9.4 T 31 cm bore Varian system with a 1.5 cm diameter single loop surface coil. The sequence was an HS1 SWIFT pulse with 25% duty cycle. The first experiment was done on 4 and 20 mM gadolinium diethylenetriamine penta-acetic acid (Gd-DTPA).The samples were diluted from a base sample and put in 5 mm glass tubes. A flip angle dependence between 0.5° and 30° for T_p = 2 and 4 ms was taken and fit to the Ernst equation. The second experiment imaged a mouse brain with a T_p = 4 ms with flip angles from 2° to 12° respectively. The data was then fit to the Ernst equations and contrast measurements were made.

3.2.2 Results and Discussion

3.2.2.1 Energy

The first objective was to compare signal energy (S^2) at constant flip angle as a function of relaxation and recovery rates. Figures 3.4 and 3.5 are S^2 contour plots for δ, on- and off-resonance hard, SWIFT, gapped SWIFT, and off-resonance SWIFT sequences at 5° and 90° plotted against T_R/T_1 and T_A/T_2. All plots are normalized to $S^2{}_{max}$ of the δ–pulse sequence at each flip angle.

$\theta = 5°$

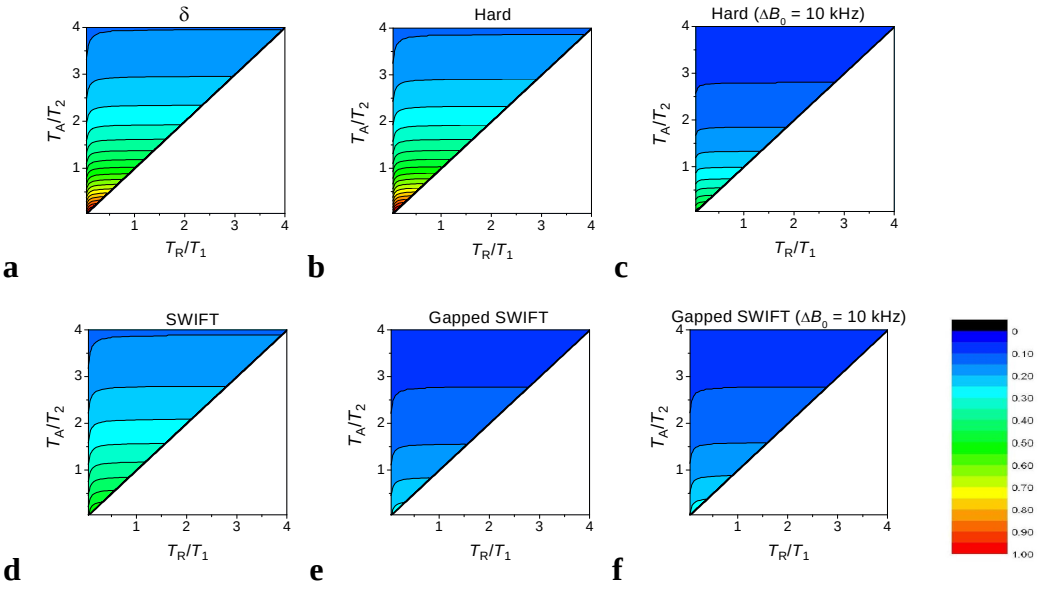

Figure 3.4: Energy (S^2) contour plots for 5° excited a) δ, b) hard, c) off-resonance hard, d) SWIFT, e) gapped SWIFT f) and off-resonance gapped SWIFT normalized to S_{max}^2 of the δ-pulse

θ = 90°

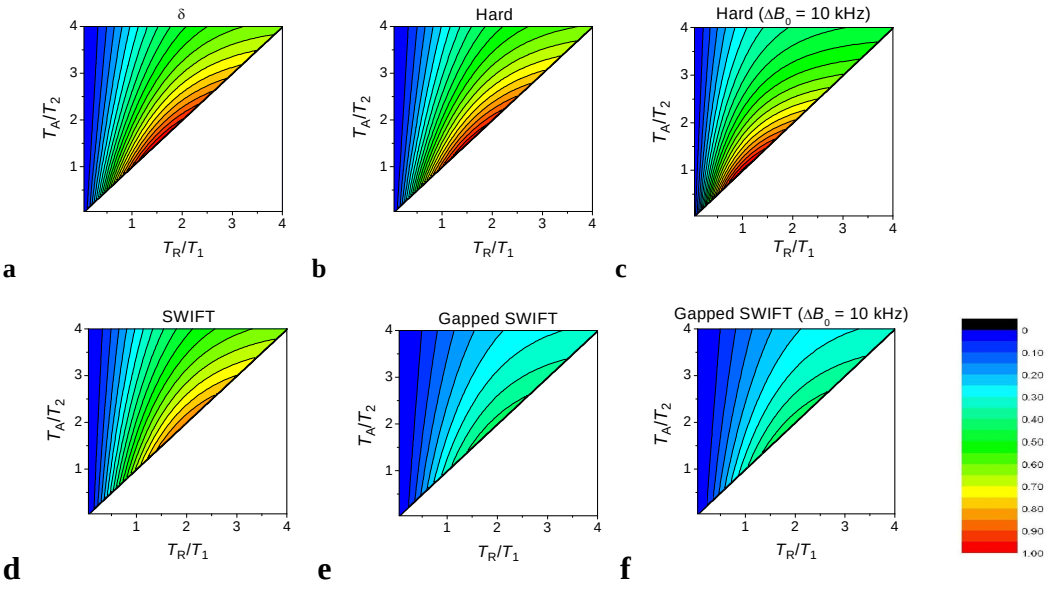

Figure 3.5: Energy (S^2) contour plots for 90° excited a) δ, b) hard, c) off-resonance hard, d) SWIFT, e) gapped SWIFT f) and off-resonance gapped SWIFT normalized to S_{max}^2 of the δ-pulse

The plots of the S^2 from the δ-sequence are the standard to which the hard and SWIFT sequence results are to be compared. The S^2 plots from the δ-sequence are described perfectly by equation 3.4. As expected, S^2 decreases as T_2 decreases at constant T_1 and S^2 increases as T_1 decreases at constant T_2. Another important feature is that there is a peak S^2 (S^2_{max}) for some value of $T_1 = T_2 = T_{1,2}$. S^2_{max} changes as a function of flip angle and $T_{1,2}$. S^2 as a function of $T_{1,2}$ is illustrated in figure 3.6a which plots the S^2 of each sequence normalized to the S^2 of the δ-sequence at 20°.

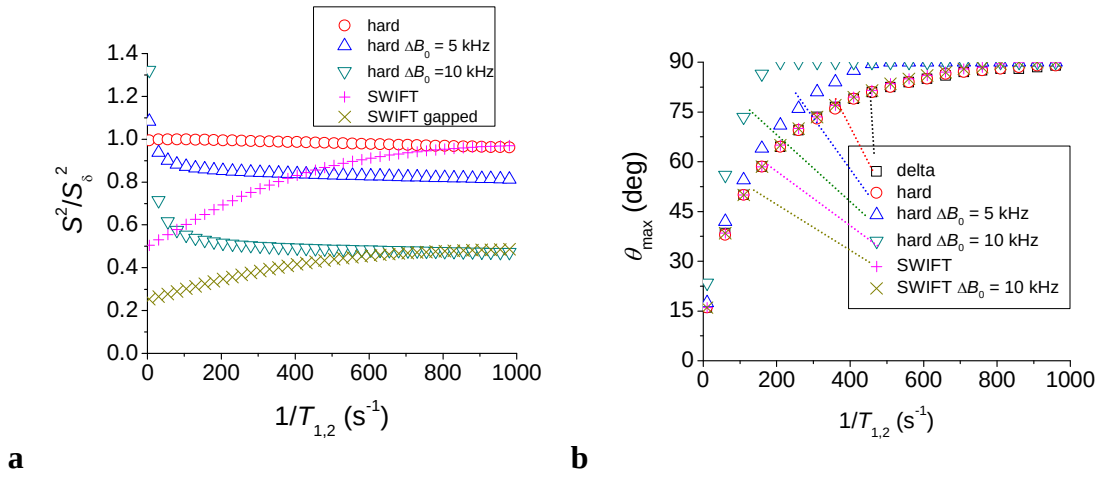

Figure 3.6: a) Normalized signal energy (S^2/S_δ^2) vs relaxation rate constant ($1/T_{1,2}$) at θ = 20° b) Flip angle (θ_{max}) of maximum signal energy (S^2_{max}) for a given $1/T_{1,2}$

The S^2 plots from the hard pulse sequence share the same T_1 and T_2 relations as the δ-sequence with a few important differences. There is some signal loss when comparing the δ and on-resonance hard sequences at short T_2. The off-resonance plots are significantly different from the on-resonance plots. The off-resonance spins reach S^2_{max} at longer $T_{1,2}$.

The S^2 plots from the SWIFT sequence do not share all of the same T_1 and T_2 relations as the δ-sequence. Continuous SWIFT has less relative S^2 for long T_2 but has equivalent S^2 for short T_2 as the δ-sequence. S^2_{max} is achieved at shorter $T_{1,2}$. Gapped SWIFT has half the S^2 as continuous SWIFT. Off-resonance SWIFT is the same as on-resonance SWIFT except with a small energy increase for long T_1 due to a slightly earlier excitation time, when the frequency is swept from positive to negative. A spin with a negative off-resonance would have a small energy decrease for long T_1 due to a slightly later excitation time.

Figure 3.6b plots the angle of maximum signal energy, the Ernst angle (θ_{max}), at a constant $T_{1,2}$. This angle is predicted by equation 3.5 for δ, hard, and all SWIFT pulse sequences. Off-resonance hard pulse sequences find the Ernst angle at a smaller flip angle than as predicted by equation 3.5.

The hard pulse sequence does not have good agreement with the Ernst equations. This is well known and is due to off-resonance effects during the pulse causing a change in the $\theta_{effective}$. There is also an energy loss during excitation due to T_2 relaxation. These effects are evident even in the ultra-short hard pulse that was used here.

SWIFT is not completely consistent with the δ–pulse sequence. This is due to the fact that for SWIFT the spin is excited approximately at the center of the pulse whereas the spin is excited immediately after the δ pulse. This creates a $T_{A\text{-effective}}$ which is ~$T_A/2$. Figure 3.7 shows that replacing T_A with $T_{A\text{-effective}}$ in equation 3.4 yields good agreement with the SWIFT results, where figure 3.7a and 3.7b are energy plots as calculated by the Ernst equations with $T_A = T_R/2$ and with continuous SWIFT simulations for $\theta = 20°$. The Ernst equations and SWIFT simulations were within 0.1% of each other for all T_1 and T_2 values. Figure 3.7c is a plot of signal energy as a function of *dc* from simulation. Signal energy scales linearly with *dc* and does not depend on T_1 and T_2. Figure 3.7d plots the percent difference between the Ernst energy equation and continuous SWIFT sequences for spins with off-resonances (ΔB_0) of -10, -5, 0, 5, and 10 kHz. The maximum difference occurs at large $T_{1,2}$. The energies become equivalent as $T_{1,2}$ becomes shorter. The largest signal loss is 4.3% for ΔB_0 = -10 kHz at $T_{1,2}$ = 1 s. The -10 kHz spin is excited at a later time than the other spins and therefore does not a acquire as much signal. The largest

signal gain is 4.2% for ΔB_0 = 10 kHz at $T_{1,2}$ = 1 s. The 10 kHz spin is excited at an earlier time than the other spins and therefore acquires more signal energy. The on-resonance spin agrees with equation 3.4. SWIFT is therefore able to be described by the Ernst equations.

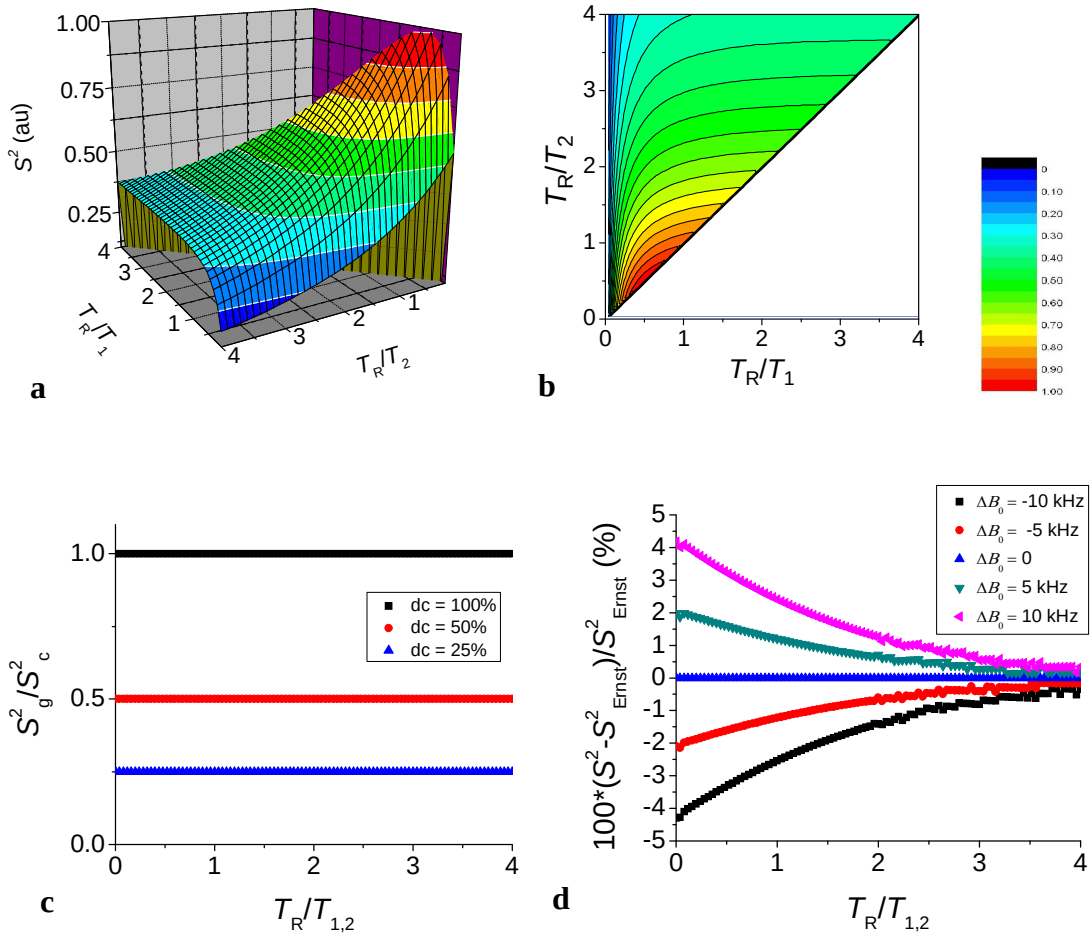

Figure 3.7: a) 3D Energy plot and b) Contour plot of continuous SWIFT and Ernst energy equation with $T_A = T_R/2$ for $\theta = 20°$. c) Gapped SWIFT energy plots for *dc* = 25, 50, and 100% normalized to continuous SWIFT energy. d) Plot of the percent difference between continuous SWIFT and the Ernst energy equation for spins with ΔB_0 = -10, -5, 0, 5, and 10 kHz.

Gapping the SWIFT pulse does not have an effect on the measured S^2 behavior, only the magnitude. Gapped and continuous SWIFT S^2 values only differ by a gapping

factor. The measured S^2 is minimally affected by the resonance of the individual spin. The slight energy increase at long T_1 is due to the slightly earlier excitation time for the off-resonance spin, when the frequency is swept from positive to negative. A spin with a negative off-resonance has a small energy decrease for long T_1 due to a slightly later excitation time.

Figure 3.8 shows the flip angle dependence of the real signal from 4 and 20 ± 1 mM Gd-DTPA when measured with SWIFT with T_p = 2 and 4 ms. The data points are fit with the Ernst equation and therefore illustrate that SWIFT experiments can be effectively described by the Ernst equations.

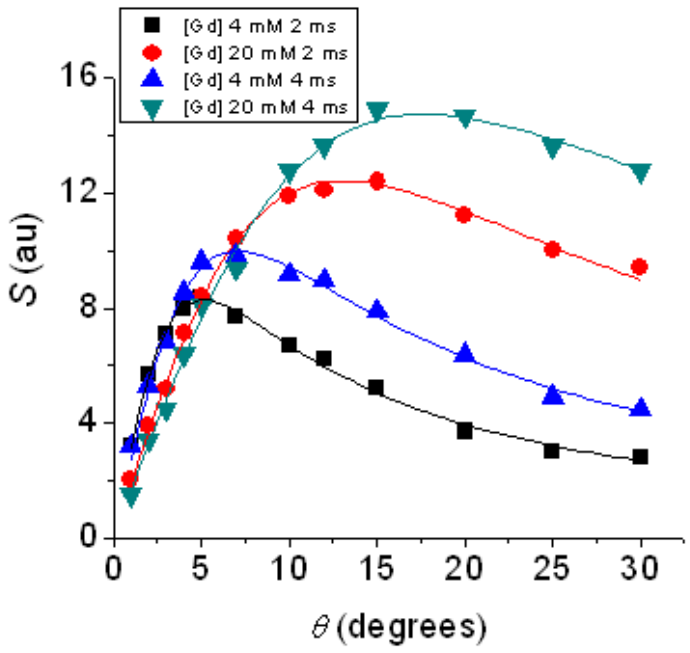

Figure 3.8: Flip angle dependence of real signal amplitude of SWIFT measured Gd-DTPA. The 4 and 20 mM samples measured at T_p = 2 and 4 ms are fit with the Ernst equation.

3.2.2.2 Maximum Energy for a Given Flip Angle

For each flip angle there is a different value of $T_{1,2}$ where S^2_{max} occurs. Figure 3.9 plots the $T_{1,2}$ value of S^2_{max} at a constant flip angle.

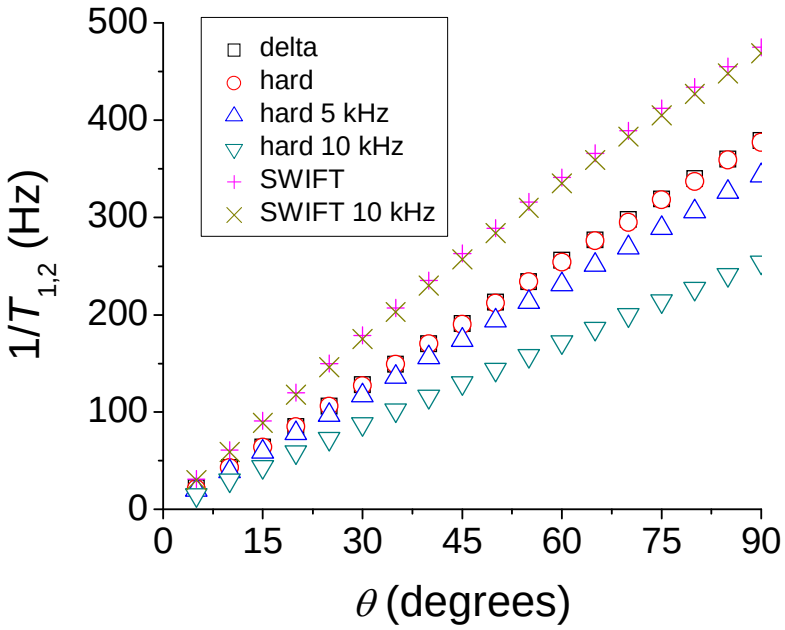

Figure 3.9: Relaxation rate constant ($1/T_{1,2}$) at which maximum signal energy occurs as function of flip angle (θ)

Contrast agents and other substances alter T_1 and T_2 values as a function of their concentration. Their relaxivities ($r_1 = C/T_1$, $r_2 = C/T_2$ mM*s)$^{-1}$ have some defined ratio r_2/r_1. Knowing this ratio, θ and T_R can be defined such that a particular concentration of contrast agent has the highest energy in the system. Figure 3.10 shows the behavior of this peak when $T_A = T_R$ and $T_A = T_R/2$ for T_R = 1, 2, 3, and 4 ms for relaxivity ratios of 1 and 2. This behavior can be calculated for $\theta < 90°$ using the equations

$$\cos(\theta) = \frac{2R\left[e^{-R}\left(1-e^{-2AR}\right)+A\left(1-e^{-R}\right)e^{-2AR}\right]-\left(1-e^{-R}\right)\left(1-e^{-2AR}\right)}{\left(\left[2R-1\right]e^{-R}\left[\left(1-e^{-R}\right)\left(1-e^{-2AR}\right)\right]+2Re^{-R}\left[e^{-R}\left(1-e^{-2AR}\right)+A\left(1-e^{-R}\right)e^{-2AR}\right]\right)} \tag{3.22}$$

$$\theta = \frac{180}{\pi}\left(\frac{T_R/T_1 + T_A/T_2}{2}\right) = \frac{180}{\pi}\left(\frac{(1+A)R}{2}\right) \tag{3.23}$$

Where $R = T_R/T_1$, $A = (T_A T_1)/(T_R T_2)$ and θ is in degrees. Equation 3.22 was solved for by taking the derivative of equation 3.4 with respect to R, setting the derivative equal to 0, and solving for θ. Equation 3.23 approximates equation 3.22 for small values of A and R. A higher order approximation is needed for other equalities. However, equation 3.22 can be used to maximize the energy of any spin in a system with known relaxivity ratio. Figure 3.10 plots the flip angle at which a particular $T_1 = AT_2$ value would have the maximum signal energy for the cases of $T_R = T_A$ and $T_1 = T_2$ (a), $T_R = 2T_A$ and $T_1 = T_2$ (b), $T_R = T_A$ and $T_1 = 2T_2$ (c), and $T_R = 2T_A$ and $T_1 = 2T_2$ (d).

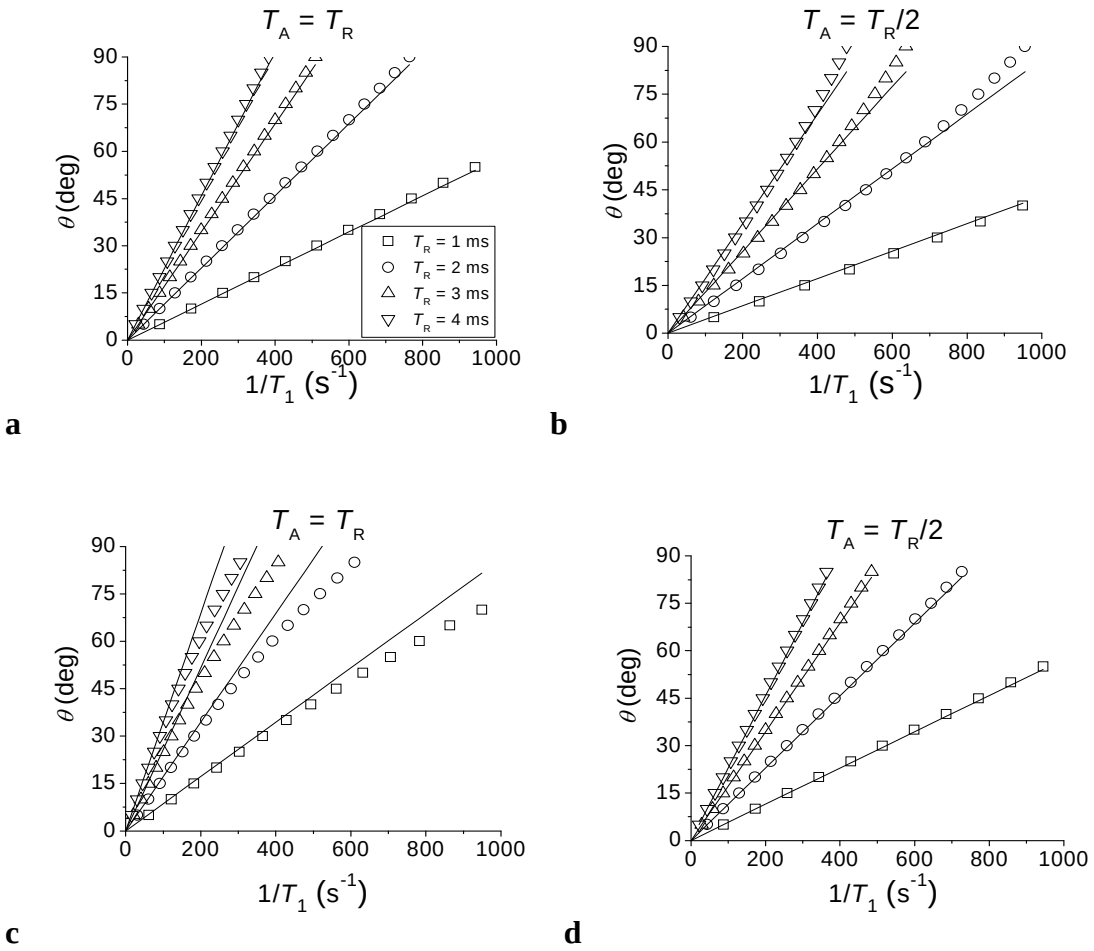

Figure 3.10: Relaxation rate constant ($1/T_{1,2}$) at which maximum signal energy occurs at a given flip angle (θ) for a) $T_R = T_A$, $T_1 = T_2$ b) $T_A = T_R/2$, $T_1 = T_2$ c) $T_R = T_A$, $T_1 = 2T_2$ d) $T_A = T_R/2$, $T_1 = 2T_2$ for T_R = 1, 2, 3, and 4 ms with lines of approximate fit of $\theta = (180/\pi)*(T_R/T_1+T_A/T_2)/2$

The experimental results in figure 3.8 illustrate the effect that the spin with maximum signal energy in the system changes as a function of flip angle. The Gd-DTPA samples are diluted from the same base sample and therefore have some relaxivity ratio. By changing the T_R the maximum energy for a given flip angle is also changed. At the lowest flip angles the 4 mM sample T_p = 2 ms has the highest signal and the 20 mM sample measured at T_p = 4 ms has the lowest signal. As the flip angle increases the signal amplitudes change such that each sample has the highest signal at some flip angle until at

the highest flip angle the 20 mM sample measured at T_p = 4 ms has the highest signal and the 4 mM sample measured at T_p = 2 ms has the lowest signal.

3.2.2.3 Contrast

It was proposed in a previous publication [9] that optimum T_1 contrast between two similarly relaxing spins can be achieved when measuring at $\theta_{opt} = 1.7\theta_{max}$. Knowing that SWIFT can be described by the Ernst energy equation allows for the use of the contrast equations derived from it, as seen in equation 3.24 [25], where E_1 corresponds to the smallest T_1 of the two compared spins.

$$\cos\left(\theta_{opt}\right) = \frac{1-2E_1}{E_1-2} \tag{3.24}$$

A mouse brain was imaged with a 1.5 cm diameter surface coil with flip angles ranging from 2° to 12°, shown in figure 3.11 a-f. The various mouse brain anatomies are clearly visible, including the cortex, hippocampus, and thalamus. The contrast and resolution allow for the distinction of fine structures, evident by the separation of the stratum pyramidale and stratum radiatum hippocampi. The images are all scaled uniformly.

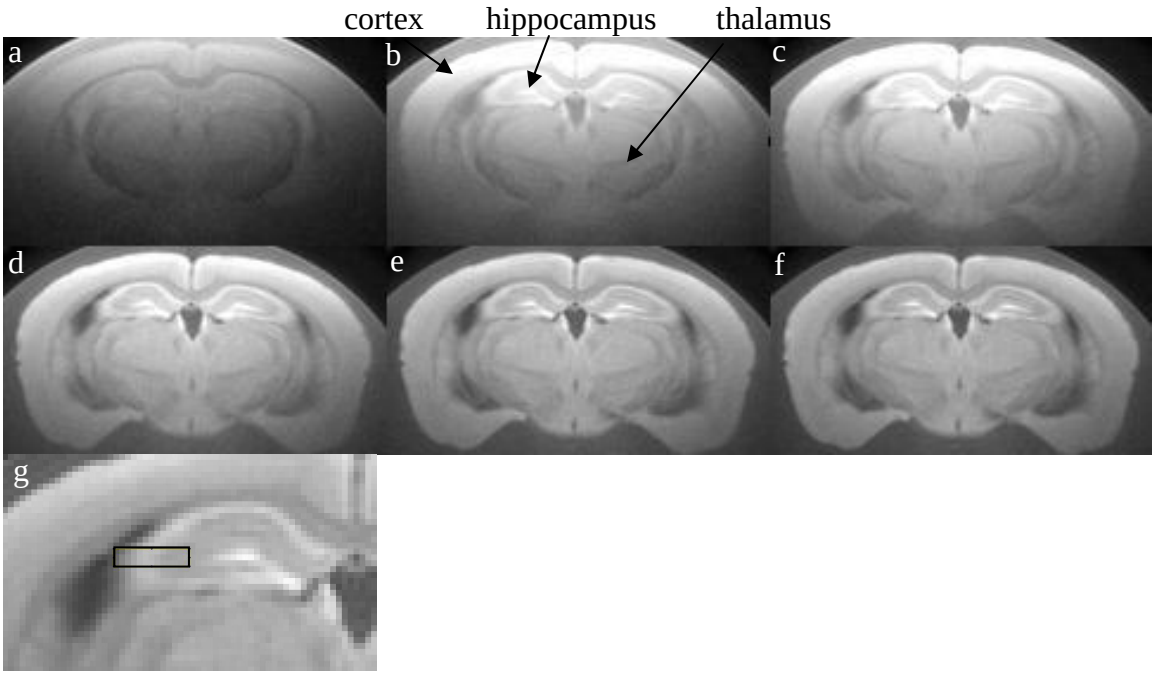

Figure 3.11: Mouse brain imaged at 9.4T with a 1.5 cm diameter surface coil at approximately 2°(a), 4°(b), 6°(c), 8°(d), 10°(e), and 12°(f). (g) is an amplification of the 10° mouse brain image with a highlighted section that includes the mouse stratum pyramidale and stratum radiatum hippocampi.

The effective flip angle changes with voxel proximity to the coil. Figure 3.12 is a calculated B_1 map [26] over the imaged area. The B_1 map was calculated by inserting a prep pulse before the SWIFT readout. The prep pulse had a constant magnitude of 44 dB, but the pulse length was varied between 0 and 500 ms. The signal amplitude of each voxel was plotted versus prep pulse duration and the curve was fit to a sinusoid. The frequency of the sinusoid is proportional to the B_1 at that voxel. The noisy regions of the B_1 map plot are where there is no signal. The black circles indicate the approximate location of the coil. The voxels closest to the coil have higher flip angles than those farther away.

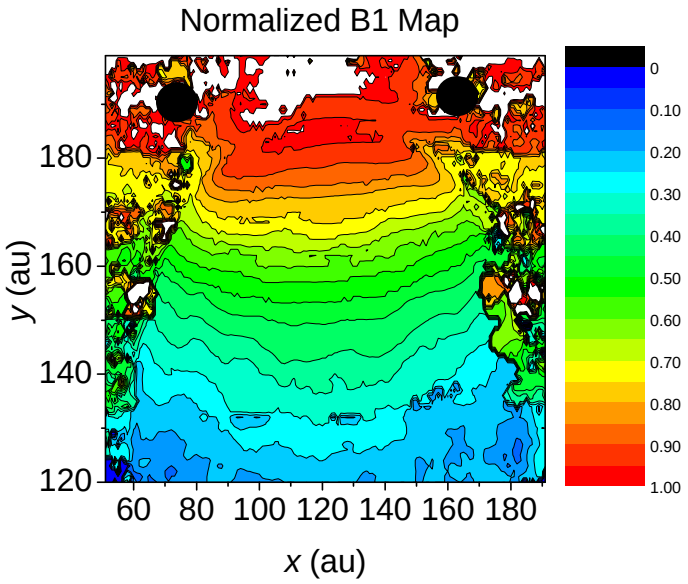

Figure 3.12: A normalized B_1 map of a surface coil over a mouse brain. The black circles indicate the approximate location of the coil.

Figure 3.11g is an amplification of the 10° flip angle image with a highlighted section over the hippocampus where the mouse stratum pyramidale and stratum radiatum hippocampi are distinguishable. The profile of the highlighted section is shown in figure 3.13 and illustrates a clear distinction between the pyramidale and radiatum anatomy where the pyramidale has higher amplitude than the radiatum. Figure 3.14 plots the signal amplitude of the anatomy as a function of effective flip angle. The data is fit to the Ernst equation. The fitting equations report T_1 values of 1.8 (pyramidale) and 2.2 (radiatum) seconds with Ernst angles of 3.77° and 3.42° respectively. Figure 3.15 plots the contrast between the signals of the anatomy with the fit line showing the contrast between the two Ernst fitting equations from figure 3.14. The maximum contrast is found to be at approximately 6.7° and is calculated from equation 3.24 as being 6.5°, which is with 2% of the$1.7\theta_{\max}$ that was previously estimated [9].

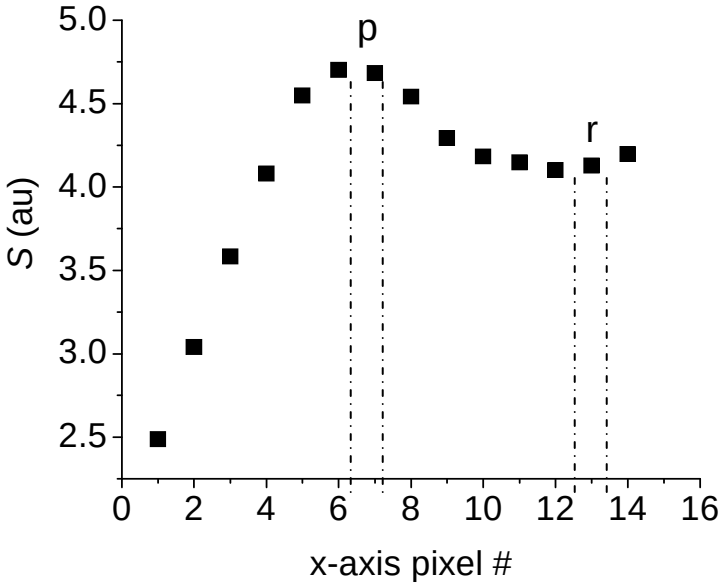

Figure 3.13: Profile of the highlighted region in figure 3.11g which includes the mouse stratum pyramidale and stratum radiatum hippocampi regions, labeled 'p' and 'r' respectively.

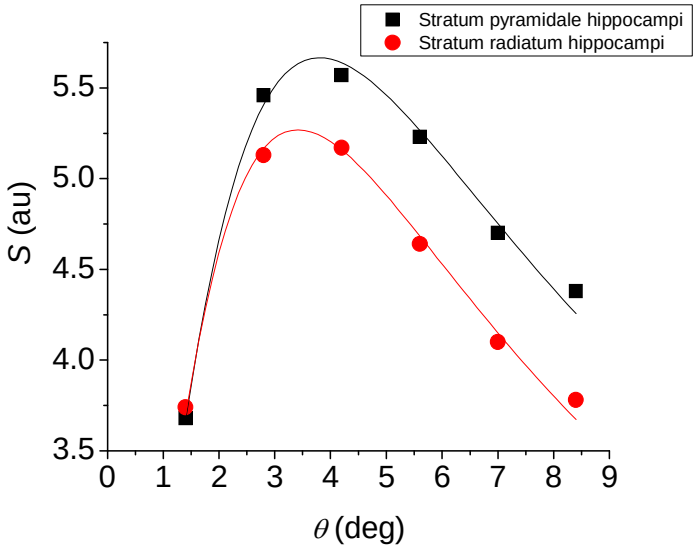

Figure 3.14: Flip angle dependence of the measured signal from the mouse stratum pyramidale (black squares) and stratum radiatum hippocampi (red circles) regions. The data points are fit with the Ernst equation.

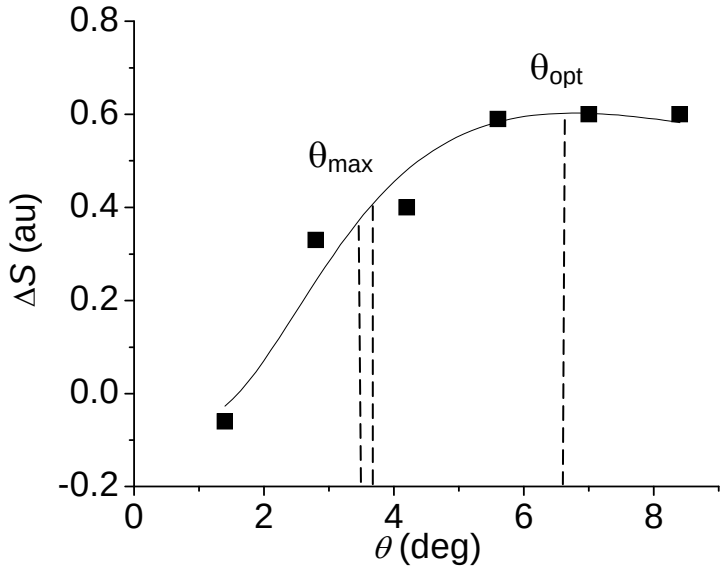

Figure 3.15: The calculated contrast (*ΔS*) from the measured signal from the mouse stratum pyramidale and stratum radiatum hippocampi regions as a function of flip angle. The fit line is calculated from the Ernst fit lines. The calculated Ernst and optimum contrast angles are marked on the plot.

3.2.2.4 Signal-to-Noise Ratio (SNR)

The SNR was evaluated for $T_2^* < T_R/2$ for several scenarios: 1) δ-pulse with 512 points over the entire T_R; 2) δ-pulse with 256 acquired points over the entire T_R; 3) δ-pulse with 256 acquired points over $T_R/2$; 4) 512-point SWIFT; and 5) gapped SWIFT (256 points). A 512 point random noise file was created using a random number generator to define the noise at each point in time with $|\sigma| \leq 0.01$. The noise was added to each FID. Each FID was Fourier transformed and the SNR was evaluated for the projected object by taking the average of the object peak and dividing by the RMS of the off-peak signal. 512-point SWIFT, 512-point δ-pulse, and δ-pulse with 256 acquired points over $T_R/2$ have equivalent SNR. Gapped SWIFT and 256-point δ-pulse both lose

a $\sqrt{2}$ in SNR. The SNR reduction occurs because even though there is an acquisition bandwidth reduction, the same noise is present. There is no signal averaging so there is no benefit to reducing the number of points taken. This is consistent with the work done by Weiger et al [27].

3.3 Conclusion

In this section is has been shown that the SWIFT sequence can be described by the Ernst energy equation with the condition $T_A = T_R/2$. SWIFT can also be described by the equations for maximum energy and contrast that are derived from the Ernst energy equation. Off-resonance spins are closely approximated by the Ernst energy equations if the varying excitation time is accounted for. Gapped SWIFT signal energy scales linearly with duty cycle (*dc*) and loses $\sqrt{dc}$ in SNR.

A new contrast method was also presented. The new method takes advantage of the relaxation rate that has maximum signal energy for given flip angle to target specific spins with $T_1 = T_2$. In a system where all spins have the same relaxivity ratio, a specific flip angle can be chosen so that a desired spin will have the highest energy in the system.

4. Superparamagnetic Iron Oxides (SPIOs)

4.1 Introduction

Superparamagnetic iron oxides (SPIOs) are used in many clinical and experimental applications. The most prevalent applications are in cancer detection and molecular imaging. SPIOs are currently used as negative contrast agents, where the T_2 shortening caused by the SPIOs is utilized to create dark spots in images. Negative contrast is not ideal because there are many areas of negative contrast in an image and it is difficult to identify the areas of SPIO. Additionally, the anatomical information in the areas of SPIO congregation is lost.

SWIFT has been shown to maintain signals that have short T_2, and therefore be able to utilize the T_1 shortening effect to create positive contrast in images. Positive contrast allows for clear identification of target areas and it retains all of the anatomical information. Figure 4.1 is a SWIFT image of 5 tubes of Feridex, one tube of water, and one tube of agar measured at 4 T with θ = 5° (a) and 14° (b). Starting with #1 and going clockwise the tubes are 0, 0.1, 0.5, 0.9, 1.9, and 4.7 mM Feridex in 0.1% agar with a water tube in the center. Feridex is a commercial ferumoxide solution with 11.4 mg of iron per mL with a core radius between 10 and 15 nm. The signal to the right of the tubes is a saline bag that was used to load the coil. The tube with water in it has the lowest signal. The signal increases with increasing Feridex concentration. The contrast is more significant in the 14° image than in the 5° image.

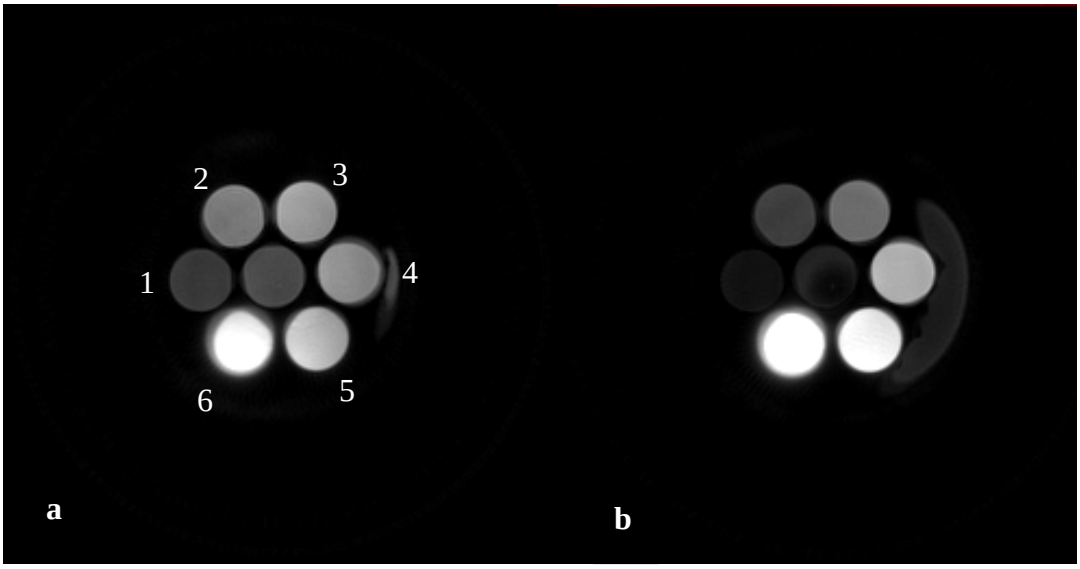

Figure 4.1: Image of tubes with 0.1% agar and, starting at #1 and going clockwise, 0, 0.1, 0.5, 0.9, 1.9, and 4.7 mM Feridex. The center tube is filled with water. The signal to the right of the tubes is a saline bag. They were measured at 4 T with θ = 5° (a) an 14° (b).

The imaging of SPIOs with SWIFT can be optimized with the equations that were determined in chapter 3. However, it is necessary to know how SPIOs change T_1 and T_2 before the sequence can be optimized. There are many parameters that need to be considered; diffusion, particle magnetization, particle size, particle concentration, and clustering are the most dominant parameters. External field strength is also an important parameter. The effects of the particle parameters change dramatically at low external field strengths; but at high fields, where we are working, the parameters will have the described effects.

4.2 Superparamagnetism

Superparamagnetic materials are nano-sized magnetic materials that have both ferromagnetic and paramagnetic properties. They are ferromagnetic materials that are too small to form domains. There is no benefit for the formation of walls to counter demagnetization energy. In the presence of a magnetic field the atomic magnetic moments will align in the direction of the applied field creating a large internal magnetic field. When there is no external field the ambient thermal energy is large enough to overcome the coupling forces between the atomic magnetic moments, causing them to dephase; bringing the net magnetization to zero. This behavior is similar to that of paramagnetism except instead of shifting singular atomic moments, the field shifts *N* moments, resulting in the magnetization as expressed in equation 4.1 [28].

$$M = \frac{N}{V} gJN\mu_B B_J\left(\frac{gJN\mu_B B_0}{k_B T}\right) \tag{4.1}$$

Where g is the Lande g factor, J is the angular momentum quantum number, μ_B is the Bohr magneton, B_0 is the external field, and B_J is the Brillouin function given in equation 4.2.

$$B_J(x) = \left(\frac{2J+1}{2J}\right)\coth\left[\frac{(2J+1)x}{2J}\right] - \left(\frac{1}{2J}\right)\coth\left[\frac{x}{2J}\right] \tag{4.2}$$

4.3 Relaxation Properties

In the presence of an external magnetic field an SPIO, approximated as a perfect sphere, will create a perfect dipole field. The secular component (parallel to B_0) of the SPIO's magnetic field is given by equation 4.3, where B_z is the magnetic field, M is the particle magnetization, r_s is the particle radius, r is the distance from the center of the

sphere, and θ is the angle from the *z*-axis. The additional field causes distortions in the otherwise homogenous field region in the magnet. [29]

$$B_z = \frac{M}{3}\left(\frac{r_s}{r}\right)^3\left(3\cos^2(\theta)-1\right) \tag{4.3}$$

Spins in the inhomogenous field region have T_1 and T_2 shortening that is diffusion, iron concentration, sphere radius, and particle clustering dependent. T_1 and T_2 shortening occurs as spins travel near the SPIO and through the inhomogeneous field. The inhomogeneous field augments the effects as described in section 2. Most of the previous work done has only considered T_2 effects because it is the dominant effect in traditional imaging techniques. However, both $1/T_1$ and $1/T_2$ are known to increase linearly with iron concentration. It has been shown that the slopes of $1/T_1$ and $1/T_2$ vs concentration curves change as a function of particle clustering. The slope of the curve decreases as the particles become more clustered because the water molecules can not diffuse as freely near clustered particles. [30]

There are two regimes of motion that are considered when evaluating the dependence on diffusion and particle radius, the static dephasing regime and the motion-averaging regime [31]. In the static dephasing regime the SPIOs and spins are all considered to be motionless. Only the effects of the inhomogenous field on the spins are considered. It is predicted that $1/T_2'$ is proportional to r_s^3 [32].

The static dephasing regime was simulated using the Bloch simulator that was previously described. Up to 5000 magnetized spheres were randomly placed in a 500x500x500 grid. The size of the particles was varied while keeping the particle iron density and the iron concentration in the system constant. Spins were located at all other

grid sites in the system. The Bloch simulator was used to evaluate the net signal of the system from a composite FID of each spin's individual FID. T_1 and T_2 were set to be infinite so that the signal decay would only be from T_2'. The signal from a single pulse was fit to an exponential curve and T_2' was extracted. Figure 4.2 is a plot of particle radius versus $1/T_2'$ from simulation data and shows the predicted cubic relation.

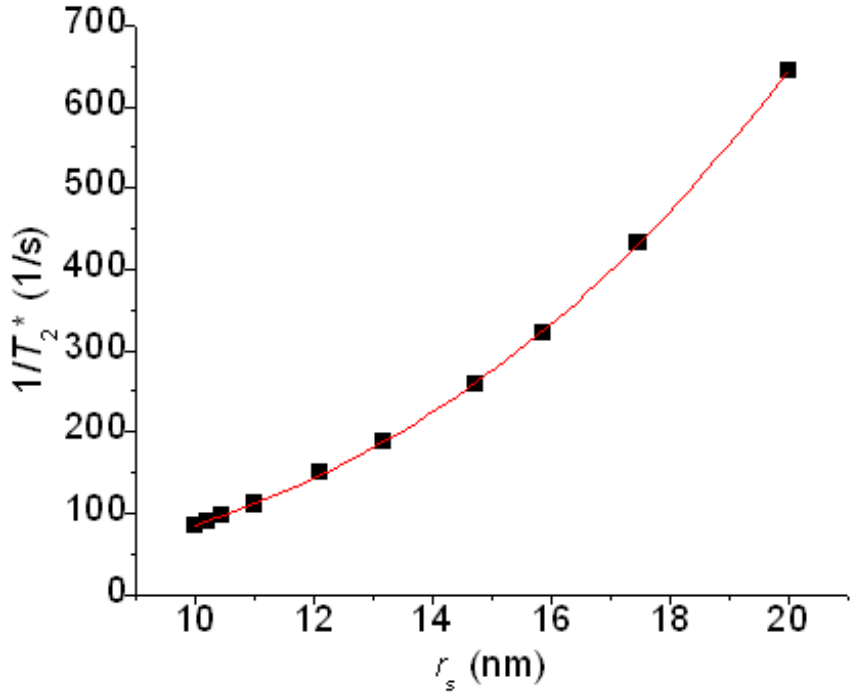

Figure 4.2: A plot of simulated data of magnetized sphere radius versus $1/T_2'$ at constant iron concentration. The data is fit to $1/T_2' = a+b*r_s^3$.

In the motion-averaging regime both the spins and the magnetized particles are allowed to move freely. The behavior of the spins is predicted well by outer sphere theory [13, 14, 15]. At high fields it is predicted that T_1 should be independent of particle radius but that $1/T_2 \sim r_s^2$. The relaxation dependence of particle radius was experimentally tested. The particles were Oleic acid-functionalized magnetite nanoparticles [33] fabricated by

Valerie Pierre's group at the University of Minnesota. All samples had 4.0 ± 0.2 mM iron but with different particle radii. The radii were 5, 7, 9, 11, 15, and 18 nm. The relaxivities ($r_1 = C_{Fe}/T_1$ and $r_2 = C_{Fe}/T_2$) were measured at 9.4 T and are plotted in figure 4.3 versus particle radius.

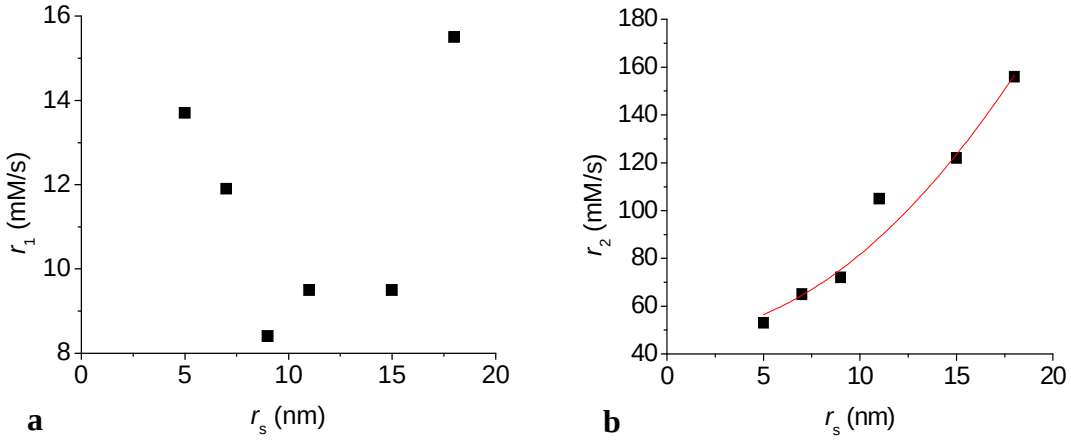

Figure 4.3: The particle radius dependence of a) r_1 and b) r_2 of 4.0 +-0.2 Mm iron oxide nanoparticles

Figure 4.3a shows that the radius dependence on r_1 appears to be uncorrelated. If the outlier at $r_s = 11$ nm is ignored then figure 4.3b shows that $r_2 \sim r_s^2$.

4.4 Optimization

The imaging of SPIOs can be optimized with the SWIFT sequence by using the Ernst equations and the equations derived from the Ernst equations. Optimization of specific SPIOs in complex systems can be achieved by using equations 3.24 for contrast and 3.5 for maximum signal energy. In phantom studies, equations 3.22 and 3.23 can be used to manipulate any SPIO system with known relaxivity ratio r_2/ r_1.

The ideal SPIO for imaging with SWIFT would have $r_1 \sim r_2$. The short T_1 would give the desired large positive contrast without being reduced by a too short T_2 effect. Equations 3.22 and 3.23 can be used to calculate the flip angle needed to ensure that the

water surrounding the SPIOs would have the highest energy in the system. If more than one concentration of SPIO is present, then the flip angle can be selected to target each individual concentration. The SPIOs would have to be specially fabricated. The primary parameter that would need to be controlled is the particle radius. r_1 is independent of r_s but is linear with concentration. r_2 increases with r_s in every motional regime and is linear with concentration. Small r_s SPIOs have small relaxivity ratios. Choice of paramagnetic material is also important, eg. Gadolinium is known to have a smaller relaxivity ratio than iron.

5. Predicting and Correcting Susceptibility Artifacts

5.1 Introduction

Metal objects cause susceptibility artifacts in magnetic resonance images. The metal objects create an inhomogenous field region that alters the Larmor frequency of the spins traveling near the object. The artifacts are caused by the inability of the Fourier transform (FT) to distinguish between spins that have the same frequency. The field gradient frequency encodes the spins in space; however the inhomogeneous field from the metal object causes spins to have duplicate frequencies. Susceptibility artifacts vary based on the size, orientation, and type of the metal object. This effect has been investigated extensively for conventional Cartesian MRI techniques [16, 17].

There are two techniques that are currently being used to correct susceptibility artifacts in images: SEMAC, slice encoding for metal artifact correction [34], and MAVRIC, multi-acquisition variable-resonance image combination [35]. The SEMAC technique adds an additional phase encoding along the *z*-direction to a VAT-SE, view angle titled spin echo, sequence. The additional phase encoding attempts to correct the phase distortion in each measured slice. SEMAC is limited to being a 2D imaging process. MAVRIC scans the object several times with different resonance frequencies. The acquisitions are then combined to create the final image. Both techniques extend acquisition times, SEMAC by extending the pulse sequence and MAVRIC by taking multiple images. SEMAC and MAVRIC both reduce susceptibility artifacts but still have signal voids and pileup artifacts.

Zhou et al. [36] investigated imaging around titanium balls (TiBs) with 3D radial gradient echo (GRE) and with 3D radial SWIFT sequences. Figure 5.1 is an image from Zhou et al.'s paper in *Magn Reson Med*, 2010. The GRE images, figures 5.1a and 5.1d, exhibited a signal void and frequency shift. The SWIFT images, figures 5.1b and 5.1e, exhibited not only a signal void but also a signal pileup artifact due to the frequency shift. In the GRE images there is significant signal loss due to the ultra-short T_2 caused by the inhomogeneous field from the TiB and long T_E of the sequence. SWIFT images, however, retain the signal in the ultra-short T_2 region and therefore are mainly affected by the frequency shift. Figure 5.1f is a plot of averaged signals from 20 adjacent slices in the SWIFT and GRE images (yellow boxes in figure 5.1 d and e). The GRE signal only had signal decay, whereas the SWIFT signal has two peaks of amplification. Figure 5.1c is the imaginary component of the SWIFT image. Only spins that are out of phase appear in the imaginary image. Here the pileup artifact is clearly visible but it is has alternating positive and negative signal that correspond to the sign of the phase shift.

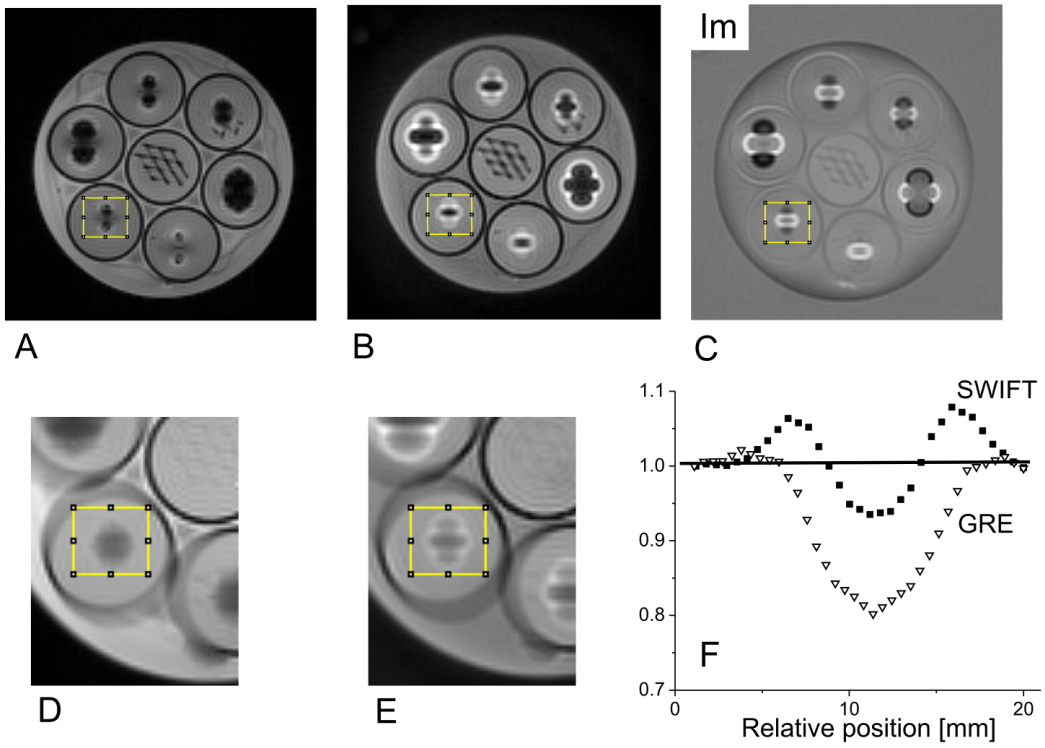

Figure 5.1: Imaging studies of a phantom consisting of a plastic jar filled with saline and seven tubes containing gelatin, TiBs, and plastic mesh. The images are a) Mag mode GRE, b) Mag mode SWIFT, and c) Im mode SWIFT. The slice shown contains the TiBs in the outer six tubes and the plastic mesh in the center tube. The balls are situated at slightly different heights; therefore, the slice shown does not cut through the center of every ball. The diameters of the TiBs in the clockwise direction starting from the top are 3.97, 2.38, 3.18, 4.76, 2.38, and 3.18 mm. The rims of the tubes are clearly identifiable from the black edge. The displaced and pileup signals around the balls are clearly visible in the SWIFT images. Expanded views of the GRE and SWIFT images obtained by averaging 20 adjacent slices are also shown with the VOI (yellow box) from which the summed profiles (f) were obtained. [taken directly from [36]]

The frequency shift for TiBs is much larger than those that will be seen from free SPIOs but a high concentration of clustered SPIOs should have the same effect. The effect for small concentrations of SPIO will also be observable, but on a much smaller scale.

5.2 Predicting Pileup Artifacts

5.2.1 Theory

In the presence of a field gradient the offset frequency from a magnetized sphere leads to a signal displacement as illustrated in the cartoon in figure 5.2 and as predicted by equation 5.1.

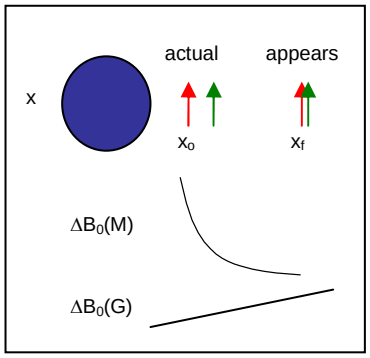

Figure 5.2: Cartoon showing how a frequency offset from a magnetized sphere causes spins to appear where they are not.

$$x_f = x_o + \frac{M}{3G}\left(\frac{r_s}{|x_o|}\right)^3\left(3\cos^2\theta - 1\right) \tag{5.1}$$

where the particle center is defined as the origin, x_o is the true position, x_f is where the spin appears in the image, M is the magnetization of the sphere, and G is the gradient strength.

The pileup will appear at the minimum of equation 5.1. Taking the derivative of equation 5.1 with respect to x_0, setting it equal to 0, solving for x_o, and plugging that value back into equation 5.1, the pileup location is then defined by equation 5.2.

$$x_{pileup} = \frac{4}{3}\left(\frac{M}{G} r_s^3 \left|3\cos^2\theta - 1\right|\right)^{1/4} \tag{5.2}$$

5.2.2 Methodology

A simulation program was written to test the result of equation 5.2. A magnetized sphere was placed at the center of a 2D map. Equation 5.1 was used to create an image by calculating the frequency at each point in space and then assigning that spin value to a compartmentalized frequency in projection space. Gradient fields were calculated for 512 discrete projections for a 512x512 map for different particle radii and magnetizations. The projections were constructed into an image by using the same reconstruction program as used in SWIFT experiments.

3D SWIFT experiments were completed on a 4T Varian system with TiB of 3/64, 1/16, 5/64, and 3/32 inch radii in 1% agar gel with Teflon mesh. The excitation bandwidth was varied from 16.7 to 125 kHz. The flip angle was adjusted to maintain a constant peak power per unit time. The magnetization of the TiB was measured using a SQUID, superconducting quantum interference device.

5.2.3 Results and Discussion

Figure 5.3a is a representative image of 6 TiB in agar gel with Teflon mesh. The sizes of the spheres in order starting at #1 and going clockwise are 5/64, 3/64, 5/64, 3/32, 1/16, and 5/64 (with mesh) inch radii. The center tube has Teflon mesh. The TiB are at slightly different depths in the tubes. Figure 5.3b is a representative 2D simulation of a TiB.

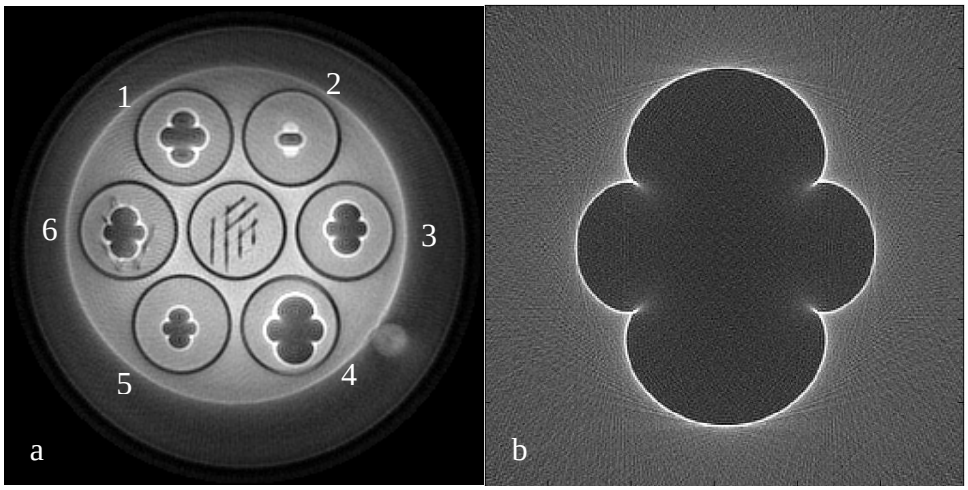

Figure 5.3: a) A representative image of experimental data at 4 T of TiB in agar gel. b) A representative image of a 2D simulation of a TiB

Figure 5.4 is a plot of the location of the furthest pileup artifact point from the center of particle #3 as a function of 1/*G*. The data points are fit to a power curve: $x = a(1/G)^b$. Similar plots and fits were done for other particles and simulation data. Table 5.1 lists the constants (*a*, *b*) obtained from plots of 1/*G* versus x_{pileup} (from the center of the particle) for the farthest pileup artifact and fitting to the equation, $x = a(1/G)^b$ for theory, simulation and experiment. The magnetization of the 1/16 inch TiB was measured to be 9.8842E-3 ± 8E-7 emu.

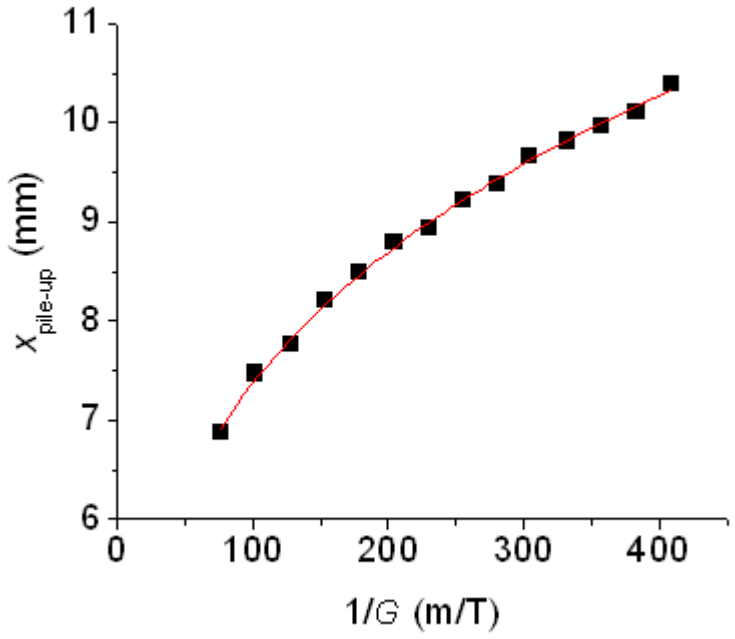

Figure 5.4: Plot of the location of the pileup artifact of particle #3 as a function of 1/*G* and fit to a power of (1/*G*)^.25

	$x = a(1/G)b$	a	b
Theory	r_s=1, M=1, θ=0	1.586	0.25
2D Simulation	r_s=1, M=1, θ=0	1.582	0.25
Experiment	r_s=1/16 inches, M=9.88E-3 emu, θ=0	0.00221	0.25
Calculated from Experimental Data	r_s=1/16 inches, M=9.88E-3 emu, θ=0	0.00208	0.25

Table 5.1: Comparison of theory, simulation, and experiment of TiB when fit with $x = a(1/G)^b$

The results in table 5.1 indicate that the analytical equation agrees very well with the simulations and experiments. In simulation, the multiplier values are within 0.3% of

the theoretical value and the power value is exactly equal to the theoretical value of 0.25. In experiment, the calculated (from measured r_s and M of a TiB) a value is within 6% of the measured value.

5.3 Correcting Pileup Artifacts

A 1D image can be reconstructed by measuring the location of the pileup artifact and by replacing the variables in equation 5.1 by the measured value, as shown in equation 5.3 where d is the distance between the pileup artifacts and the predicted center of the sphere.

$$x_f = x_o + \frac{\left(\frac{3}{4}d\right)^4}{3\left|x_o^3\right|} \tag{5.3}$$

Since the relationship between where spins are and where they were moved from is known, the spins can be moved back to approximately where they belong. The process is begun by defining the center of the particle as the origin. Using equation 5.3, x_f is calculated for each x_o and rounded to a discrete location. The total signal at each x_f location is divided by the number of spins moved to that location and the normalized signal is assigned to the x_o locations. Spins that are shifted outside of the field of view are assigned a zero signal at x_o.

An experiment was completed at 9.4 T. A 5 mm glass tube was filled with agar gel with a 1/16 inch radius TiB in the center. The TiB fit snugly in the tube. The tube was placed in the center of a 1.5 cm diameter single loop coil with the TiB in the center of the loop. Figure 5.5 is a SWIFT image of the sample with field of view of 8x8x8 cm, bw = 125 kHz, $\theta = 4°$, in steady state. It is a reference image to show orientation, size, and the

existence of the pileup artifact. The sphere is in the center of the signal void, in between the pileup artifacts.

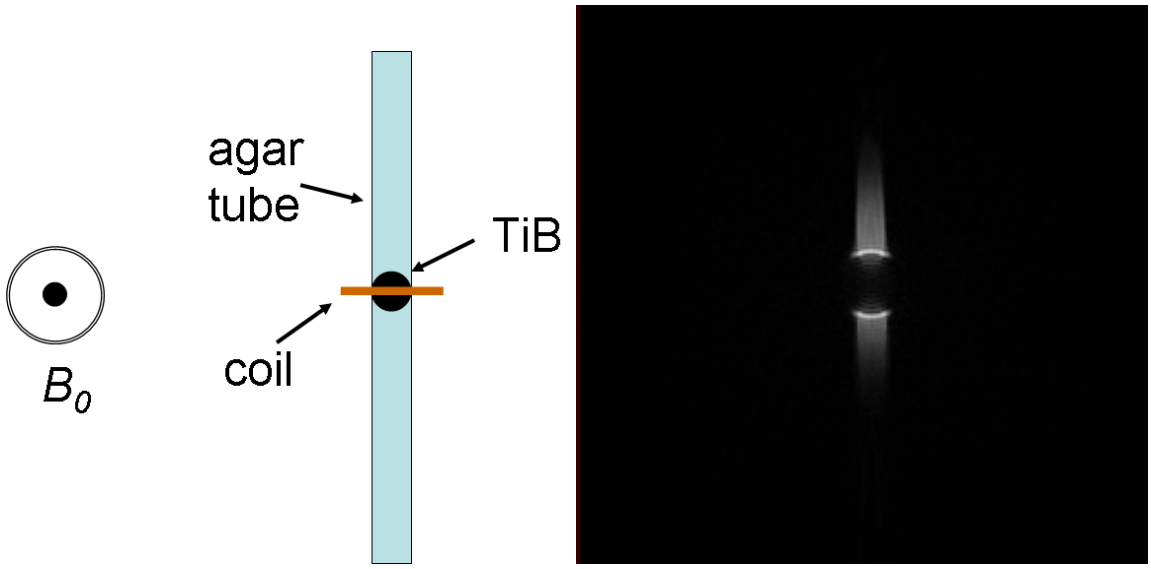

Figure 5.5: An agar tube with a TiB in the center imaged at 9.4 T with θ = 4° and bw = 125 kHz. The field of view is 8x8 cm. The B_0 field is perpendicular to the tube.

Figure 5.6 is a plot of a single pulse single projection image in a pseudo 1D experiment. The field of view was 30x3x30 cm in order to have the sample be on approximately a single line in the image. The black squares are the acquired signal with a distinctive pileup artifact. The red circles are the reconstructed data using the method described above. The pile-up artifact is no longer evident and the location of the particle is marked by the zero points of signal in the center. The signal is symmetric around the TiB. The edges around the void are curved because it is not a pure 1D experiment along a single angle radially from the TiB. The signal area has a thickness that is equal to the diameter of the sphere and extends the length of the tube in agar.

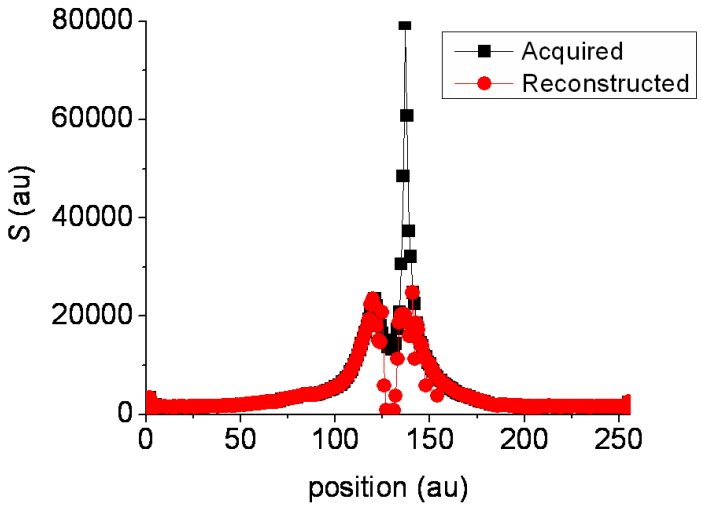

Figure 5.6: A plot of a pseudo 1D image of the TiB in Agar. The black squares are the acquired data. The red circles are the data after reconstruction.

The radial off-resonance correction (ROC) technique can be extended to correct a 3D image. Each projection in the image needs to be corrected in the same way as the 1D image except the frequency offsets in all of 3D space need to be calculated and adjusted for based on gradient orientation.

6. Conclusions

This work has shown that SWIFT signals can be accurately described by the Ernst equations. The signal from SPIOs or any other object can be optimized through judicious use of the Ernst energy equation and the equations derived from it, as listed in table 4.1. Imaging with SWIFT is more efficient if the relaxation constants are known or relaxation constants can be derived from images if they are not known.

Ernst Angle: Angle of maximum signal energy for a given spin $\cos(\theta_{\max}) = \mathrm{e}^{-T_R/T_1}$
Angle of maximum contrast between spins with similar T_1 $\cos\left(\theta_{opt}\right) = \frac{1-2\,\mathrm{e}^{-T_R/T_1}}{\mathrm{e}^{-T_R/T_1}-2}$
Relaxation rate of maximum signal energy for a given flip angle: Can be used to define a flip angle where a spin with given A has the highest energy in the system. $\cos(\theta) = \frac{2R\left[e^{-R}\left(1-e^{-2AR}\right)+A\left(1-e^{-R}\right)e^{-2AR}\right]-\left(1-e^{-R}\right)\left(1-e^{-2AR}\right)}{\left(\left[2R-1\right]e^{-R}\left[\left(1-e^{-R}\right)\left(1-e^{-2AR}\right)\right]+2Re^{-R}\left[e^{-R}\left(1-e^{-2AR}\right)+A\left(1-e^{-R}\right)e^{-2AR}\right]\right)}$ Approximation of the relaxation rate of maximum signal energy for a given flip angle equation: only good for small A and R values. $\theta = \frac{180}{2\pi}\left(\frac{T_R}{T_1}+\frac{T_A}{T_2}\right) = \frac{180}{2\pi}\left(1+A\right)R$ where $R = T_R/T_1$ and $A = T_A T_1/T_R T_2$.

Table 6.1: A list of equations that can be used to optimize SWIFT imaging.

Current SPIOs are designed to have ultra-short T_2. In the future, SPIOs should be tailored to be imaged by SWIFT because the positive contrast obtained with SWIFT is more informative than the negative contrast that is obtained with other techniques. Conventional sequences require ultra-short T_2 to obtain their desired negative contrast. SWIFT images benefit from the effects of short T_1 to obtain positive contrast. SPIOs should be created so that T_1 is approximately equal to T_2; which occurs for particles with

small radii and at low field strengths, but might also be possible through other techniques. With $T_1 \sim T_2$, the flip angle can be manipulated, using the relaxation rate of maximum signal energy equations given in table 6.1, so that the SPIO has the highest energy in the system, and therefore the brightest points in space.

The pileup artifacts that surround metallic objects in SWIFT images are predictable and can be corrected. This work showed as an example that the ROC, Radial Off-resonance Correction, technique can be used to correct artifacts around metal spheres. The ROC technique can be extended to metal objects of other shapes and can be used on clustered SPIOs or even single voxel displacements. The ROC technique is powerful because it is done in post-processing, so that no additional images or longer scan times are needed as in other techniques. In the future it will be extended to correct 3D images. The ROC technique could become very important in medical imaging because there are a limited variety and geometry of metal objects that are intentionally inserted into the human body. The field maps from those objects can be predetermined and then the images can be post processed, removing all artifacts from patient movement and reducing patient scan times.

The imaginary SWIFT image can also be used as a tool to determine if an object is paramagnetic or diamagnetic. In the imaginary image, spins that have a positive off-resonance exhibit a dark signal whereas spins that have a negative off-resonance exhibit a bright signal. A paramagnetic object will have negative signal in the direction of the external magnetic field and a diamagnetic object will have a positive signal. This allows for applications such as determining if positive contrast comes from a calcification or an air bubble. [37]

7. References

1. Hafner, *Fast imaging in liquids and solids with the back-projection low angle shot (BLAST) technique*. Magn Reson Imaging **12**,1047-1051 (1994)

2. Madio, Lowe, *Ultra-fast imaging using low flip angles and fids*. Magn Reson Med **34**, 525-529 (1995)

3. Bergin, Pauly, Macovski, *Lung parenchyma: Projection reconstruction*, MR imaging. Radiology, **179**, 777-781 (1991)

4. Robson, Gatehouse, Bydder, Bydder, *Magnetic resonance: An introduction to ultrashort TE (UTE) imaging*. J Comput Assist Tomogr **27**, 825-846 (2003)

5. Wu, Ackerman, Chesler, Graham, Wang, Glimcher, *Density of organic matrix of native mineralized bone measured by water- and fat-suppressed proton projection*, MRI. Magn Reson Med **50**, 59-68 (2003)

6. Enid, Creyghton, *High resolution NMR imaging in solids*. Physica B **125**, 81-83 (1985)

7. Jezzard, Attard, Carpenter, Hall, *Nuclear magnetic resonance imaging in the solid-state*. Prog NMR Spectrosc **23**, 1-41 (1991)

8. Balcom, MacGregor, Beyea, Green, Armstrong, Bremner. *Single-point ramped imaging with T_1 enhancement (SPRITE)*. J Magn Reson A **123**, 131-134 (1996)

9. Idiyatullin, Corum, Park, Garwood, *Fast and quiet MRI using a swept radiofrequency* J. Magn. Reson. **181**, 1-8 (2006)

10. Idiyatullin, Corum, Moeller, Garwood, *Gapped Pulses for Frequency-Swept MRI*, JMR **193**, 267-273 (2008)

11. Boulant, *T_1 and T_2 effects during radio-frequency pulses in spoiled gradient echo sequences,* J. Magn. Reson. **197**, 213-218 (2009)

12. Ernst, Bodenhausen, Wokaun. *Principles of Nuclear Magnetic Resonance in One and Two Dimensions*, Oxford Sci. Pub., **153**, 119-124, (1987)

13. Gueron, *Nuclear Relaxation in Macromolecules by Paramagnetic Ions: A Novel Mechanism,* J. Magn. Reson. **19**, 58-66 (1975)

14. Gillis, Roch, Brooks, *Corrected Equations for Susceptibility-Induced T2-Shortening*, J. Magn. Reson. **137**, 402-407 (1999)

15. Roch, Muller, Gillis, *Theory of proton relaxation induced by superparamagnetic particles*, J. Magn. Reson. **110**, 5403-5411 (1999)

16. Posse, Aue, *Susceptibility Artifacts in Spin-Echo and Gradient-Echo Imaging*, J. Magn. Res. **88**, 473-492 (1990)

17. Zabow, Dodd, Shapiro, Moreland, Koretsky, *Microfabricated High-Moment Micrometer-Sized MRI Contrast Agents*, Mag. Res. Med., **65**, 645-655. (2011)

18. Levitt, Malcolm. (2001). *Spin Dynamics*, New York, Wiley

19. Garwood, DelaBarre, *The Return of the Frequency Seep: Designing Adiabatic Pulses for Contemporary NMR*, JMR **153**, 155-177 (2001)

20. Beatty, Nishimura, Pauly, *Rapid Gridding Reconstruction with a Minimal Oversampling Ratio*, IEEE Trans. Med. Imag. **24**, no. 6, 473-478 (2005)

21. Szantay, *Evolution of Magnetization in a B1 Field. I. The Impact of B0/B1 Inhomogeneity and Fast Chemical Exchange in High-Resolution NMR*, Concepts in Mag. Res. **11**, 343-362 (1999)

22. Ernst, Bodenhausen, Wokaun. *Principles of Nuclear Magnetic Resonance in One and Two Dimensions*, Oxford Sci. Pub. **153**, 119-124, 1987

23. Liimatainen, Sorce, O'Connell, Garwood, Michaeli, *MRI Contrast From Relaxation Along a Fictitious Filed (RAFF)*, Mag. Res. Med., **64**, 983-994 (2010)

24. Gerald, Wheatley, (1985) *Applied Numerical Analysis: Third Edition*, Reading Massachusetts, Addison-Wesley Publishing Company, p. 310

25. Buxton, Edelman, Rosen, Wismer, Brady, *Contrast in Rapid MR Imaging: T1-and T2-Weighted Imaging*, J. Comp. Assisted Tomog., **11**, 7-16 (1987)

26. Vaughan, Garwood, Collins, Liu, DelaBarre, Adriany, Andersen, Merkle, Goebel, Smith, Ugurbil, *7T vs. 4T: RF Power, Homogeneity, and Signal-to-Noise Comparison in Head Images*, Mag. Res. Med., **46**, 24-30 (2001)

27. Weiger, Pruessmann, Hennel, *MRI with Zero Echo Time: Hard versus Sweep Pulse Excitation*, Mag. Res. Med. (2011)

28. O'Handley, (2000) *Modern Magnetic Materials: Principals and Applications*, New York,Wiley

29. Jackson, (1999) *Classical Electrodynamics*, New York, Wiley

30. Tanimoto, Oshio, Suematsu, Pouliquen, Stark, *Relaxation Effects of Clustered Particles*, J. Magn. Reson. Imag. **14**, 72-77 (2001)

31. Gillis, Moiny, Brooks, *On T2-Shortening by Strongly Magnetized Spheres: A Partial Refocusing Model*, Mag. Res. Med., **47**, 257-263 (2002)

32. Bowen, Zhang, Saab, Gareau, Rutt, *Application of the Static Dephasing Regime Theory to Superparamagnetic Iron Oxide Loaded Cells*, Mag. Res. Med., **48**, 52-61 (2002)

33. Sun, Zeng, Robinson, Raoux, Rice, Wang, Li. *Monodisperse MFe_2 O_4 (M = Fe, Co, Mn) Nanoparticles*. J. Am. Chem. Soc., **126**, 273-279. (2004)

34. Lu, Pauly, Gold, Pauly, Hargreaves, *SEMAC: Slice Encoding for Metal Artifact Correction in MRI*, Mag. Res. Med., **62**, 66-76 (2009)

35. Koch, Lorbiecki, Hinks, King, *A Multispectral Three-Dimensional Acquisition Technique for Imaging Near Metal Implants*, Mag. Res. Med., **61**, 381-390 (2009)

36. Rong, Idiyatullin, Moeller, Corum, Zhang, Qiao, Zhong, Garwood, *SWIFT Detection of SPIO-Labeled Stem Cells Grafted in the Myocardium*, Mag. Res. Med., **63**, 1154-1161 (2010)

37. Lehto, *Calcification Imaging with SWIFT in Rat Brain*, proceedings at ISMRM 2011